Biophysical Journal
Article

Biophysical Society

NAD(P)H binding configurations revealed by time-resolved fluorescence and two-photon absorption

Thomas S. Blacker,[1,2] Michael R. Duchen,[2] and Angus J. Bain[1,*]
[1]Department of Physics & Astronomy, University College London, London, United Kingdom and [2]Research Department of Cell & Developmental Biology, University College London, London, United Kingdom

ABSTRACT NADH and NADPH play key roles in the regulation of metabolism. Their endogenous fluorescence is sensitive to enzyme binding, allowing changes in cellular metabolic state to be determined using fluorescence lifetime imaging microscopy (FLIM). However, to fully uncover the underlying biochemistry, the relationships between their fluorescence and binding dynamics require greater understanding. Here we accomplish this through time- and polarization-resolved fluorescence and polarized two-photon absorption measurements. Two lifetimes result from binding of both NADH to lactate dehydrogenase and NADPH to isocitrate dehydrogenase. The composite fluorescence anisotropy indicates the shorter (1.3–1.6 ns) decay component to be accompanied by local motion of the nicotinamide ring, pointing to attachment solely via the adenine moiety. For the longer lifetime (3.2–4.4 ns), the nicotinamide conformational freedom is found to be fully restricted. As full and partial nicotinamide binding are recognized steps in dehydrogenase catalysis, our results unify photophysical, structural, and functional aspects of NADH and NADPH binding and clarify the biochemical processes that underlie their contrasting intracellular lifetimes.

SIGNIFICANCE The metabolic cofactors NADH and NADPH exhibit spectrally identical fluorescence, labeled NAD(P)H. The fluorescence lifetime of NAD(P)H is sensitive to shifts in metabolism, raising hope that FLIM could be used to determine the metabolic pathways active within the cells of living tissues. However, little is known about how the cofactor photophysics are mediated by the enzymes to which they bind, making NAD(P)H FLIM measurements difficult to interpret. Here we show that two distinct binding configurations, in which the nicotinamide chromophore either retains conformational freedom or becomes fully bound, are associated with distinct fluorescence lifetimes. These represent key steps in the dehydrogenase catalytic mechanism, demonstrating influence on NADH and NADPH fluorescence by the kinetics of the metabolic reactions they facilitate.

INTRODUCTION

The intracellular pools of nicotinamide adenine dinucleotide (NAD) and its phosphorylated analogue NADP are responsible for ferrying reducing equivalents between the redox reactions of metabolism (1). Their reduced forms (NADH and NADPH) are fluorescent, emitting at 460 ($\pm$50) nm after excitation at 340 ($\pm$30) nm, an absorption band that is absent when oxidized to NAD+ and NADP+ (2). The phosphate group that differentiates the two molecules allows enzyme binding sites to be specific to either cofactor, enabling their regulation of distinct sets of metabolic reactions (3). NAD is primarily involved in catabolic pathways in which molecules are broken down to provide energy in the form of adenosine triphosphate (ATP), such as glycolysis in the cytosol and the tricarboxylic acid (TCA) cycle in the mitochondria. In contrast, NADP primarily contributes to biosynthetic processes such as the production of lipids and nucleic acids and the maintenance of the glutathione and thioredoxin defenses against reactive oxygen species (ROS) (1).

The absorption and emission characteristics of NADH and NADPH are identical as the additional phosphate group is distant from the nicotinamide chromophore (Fig. 1) (1,2,4). The spectrally indistinguishable endogenous fluorescence

Submitted April 13, 2022, and accepted for publication February 10, 2023.

*Correspondence: a.bain@ucl.ac.uk

Thomas S. Blacker's present address is Research Department of Structural & Molecular Biology, University College London, London, United Kingdom.

Editor: Jochen Mueller.

https://doi.org/10.1016/j.bpj.2023.02.014

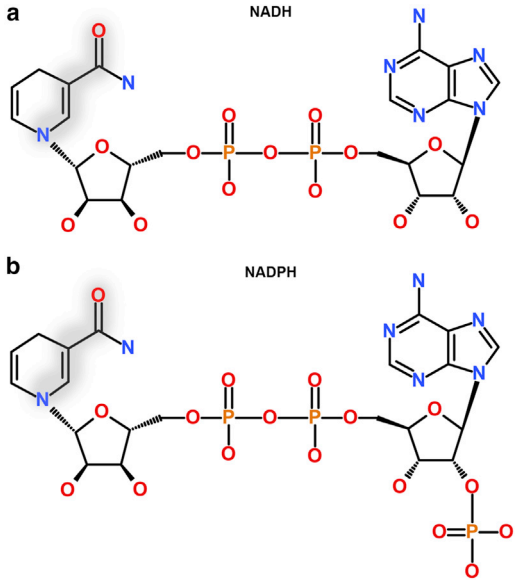

Web 3C

FIGURE 1 NADH and NADPH are intrinsically fluorescent, structurally similar enzymatic cofactors that regulate contrasting sets of redox reactions within the cell. Absorption and emission are localized to the nicotinamide ring of both molecules, with the transition involving transfer of charge between the ring nitrogen to the oxygen of the amide group, shown in gray. NADPH (*b*) differs from NADH (*a*) only by the presence of a phosphate group at the adenine end of the molecule. Although the distance of this group from the chromophoric region results in identical photophysics of the molecules when isolated in solution, its negative charge allows enzyme binding sites to be specific for either cofactor. This allows NADH to regulate ATP-generating catabolic pathways, whereas NADPH is primarily involved in biosynthesis. To see this figure in color, go online.

of these molecules, labeled NAD(P)H (1), has been used to report the metabolic state of living cells and tissues since the 1950s (5). The lack of any fluorescence signal from oxidized NAD(P)+ allows changes in the NAD(P)H intensity to be directly correlated to the redox balance within a biological sample (1). Such measurements were crucial in early investigations of the mitochondrial electron transport chain (ETC) (6) and continue to be applied to this day using laser scanning confocal microscopy in the study of mitochondrial dysfunction (7,8). The commercialization of fluorescence lifetime imaging microscopy (FLIM) in the 1990s enabled work demonstrating the sensitivity of time-resolved NAD(P)H fluorescence to changes in the metabolic state of living samples (9). This was widely observed to contain two components, one with a short lifetime (~0.4 ns) representing freely diffusing cofactors and one with a longer lifetime (2–4 ns) arising from enzyme-bound species (1). Both the average bound lifetime and the proportion of bound to free NAD(P)H change in response to metabolic perturbations (10–14). This has prompted the development of FLIM-based diagnostic tools (15) to exploit the close links between metabolism and pathology (16). However, both the clinical application of these and use of NAD(P)H FLIM to rigorously interrogate pathophysiological processes have been held back by inadequate knowledge of the molecular mechanisms that connect metabolic state with NAD(P)H lifetime (1). Key to rectifying this is to understand how metabolic enzyme binding perturbs the photophysics of these cofactors.

We have demonstrated that changes in the fluorescence lifetime of the enzyme-bound NAD(P)H population reflect changes in the balance of NADPH and NADH (17). This allowed us to use FLIM to separately investigate the roles of the two cofactors for the first time, in diseases ranging from hearing loss (18) and cancer (19) to heart disease (20) and diabetes (21). Our results indicated that the separate binding sites of NADH and NADPH give rise to contrasting fluorescence lifetimes, which we predicted to be 1.5 ($\pm$0.2) ns and 4.4 ($\pm$0.2) ns respectively (17); however, the underlying mechanisms were unclear. We have recently studied the relationships between the fluorescence and conformational dynamics of NADH and NADPH in solution using polarized two-photon absorption and time-resolved intensity and anisotropy measurements. This demonstrated that small-scale motion of the nicotinamide ring and alterations to its geometry mediate their lifetimes (22,23). Here, we extend these investigations to study the fluorescence dynamics of NADH and NADPH when bound to two corresponding enzymes. These reveal heterogeneous fluorescent populations resulting from distinct binding configurations associated with the "open" and "closed" dehydrogenase conformational states.

METHODS

NAD(P)H and enzyme solutions

NADH and NADPH were obtained from Sigma-Aldrich (Dorset, UK). Recombinant human lactate dehydrogenase (UniProtKB: P07195) and isocitrate dehydrogenase (UniProtKB: O75874), expressed in *Escherichia coli* and chromatography purified (>95% SDS-PAGE), were supplied by Abcam (Cambridge, UK). These were resuspended in 5 mL of 10 mM pH 7.4 Tris buffer (Sigma-Aldrich, Dorset, UK) containing 10 μM NADH or NADPH, and concentrated by spinning for 15 min at 2000 × *g* in a 10-kDa molecular weight cutoff Amicon Ultra-4 centrifugal filter unit (Merck, Watford, UK). Resuspension and centrifugation were repeated a further two times to ensure negligible presence of the original enzyme buffer. The final volume of the enzyme and cofactor mixture was between 90 and 100 μL. The mixtures were placed in a 50-μL, 3-mm path length quartz cuvette for measurements (Hellma, Southend on Sea, UK). Ternary complexes were produced by adding 10 μL of 1 mM sodium lactate or sodium isocitrate into the experimental sample, giving a final substrate concentration of at least 100 μM to ensure negligible levels of binary NAD(P)H-enzyme complexes.

Laser sources

Single-photon excitation at 340 nm was achieved by frequency doubling the 680-nm output of a tunable optical parametric amplifier (OPA 9400, Coherent, Cambridge, UK) using a β-barium borate

(BBO) crystal. The OPA was pumped by a regeneratively amplified Ti:sapphire laser (Mira 900F and RegA 9000, Coherent, Cambridge, UK) operating at 800 nm with a repetition rate of 250 kHz, in turn pumped by an Nd:YVO_4 laser (Verdi V18, Coherent, Cambridge, UK). The direct output of the OPA at 690 nm was used for two-photon fluorescence measurements.

Polarized time-correlated single-photon counting

Linearly polarized excitation was implemented by passage through a half-wave plate and Glan-Laser polarizer (Melles-Griot, New York, USA). A zero-order tunable quarter wave plate (Alphalas, Goettingen, Germany) was introduced for circularly polarized two-photon excitation (23). A 25-mm focal length achromatic doublet lens (Melles-Griot, New York, USA) was used to focus the polarized beam onto the sample cuvette. Fluorescence was collected in a 90° excitation-detection geometry by using a 25-cm focal length lens to direct the emission into a multichannel plate photomultiplier tube (MCP-PMT, R3809U, Hamamatsu Photonics, Welwyn Garden City, UK). 364-nm long-pass (BLP01-364R-25, Semrock, New York, USA) and 600-nm short-pass (BG39, Schott, Stafford, UK) filters were used to eliminate laser breakthrough during single- and two-photon excitation respectively. A modular time-correlated single-photon counting (TCSPC) system (Ortec, Oak Ridge, USA) was used for time- and polarization-resolved fluorescence measurements. A computer-controlled rotatable polaroid sheet was used to select the polarization of the collected fluorescence. This was alternated at 10-s intervals to transmit light polarized parallel or perpendicular to the symmetry axis of the excitation polarization (vertical for linear, horizontal for circular) (23). The corresponding decays, $I_{\parallel}(t)$ and $I_{\perp}(t)$, were built up from excitation-detection coincidence events allocated to 512 time bins spanning 27 ns and stored separately in computer memory.

For single-photon excitation, the incident intensity was reduced using an adjustable neutral density filter wheel to ensure average count rates below 2.5 kHz to avoid pulse pile-up effects. Excitation-emission coincidence events were collected for approximately 30 min, resulting in approximately 3×10^6 total photons collected. For two-photon excitation, count rates were around a factor of 40 lower. Data collection times were extended to an hour, resulting in approximately 10^5 photons per decay. Fluorescence intensity decays were constructed using

$$I(t) = I_{\parallel}(t) + 2I_{\perp}(t) \tag{1}$$

In the case of circularly polarized excitation, the symmetry axis is the direction of propagation of the excitation pulses and the fluorescence intensity is determined from (23),

$$I_{\mathrm{circ}}(t) = 2I_{\parallel}(t) + I_{\perp}(t) \tag{2}$$

For linearly polarized excitation, the time-resolved fluorescence anisotropy was calculated from

$$R(t) = \frac{I_{\parallel}(t) - I_{\perp}(t)}{I_{\parallel}(t) + 2I_{\perp}(t)} \tag{3}$$

Fluorescence intensity and anisotropy decay fitting

The instrument response function (IRF) of our TCSPC system was measured, revealing an FWHM of 74 ps (Fig. S1). Its influence was therefore neglected in the analysis of our intensity and anisotropy decay measurements, given that this is significantly faster than the typical ~400-ps (22) fluorescence lifetime and rotational correlation time of freely diffusing NAD(P)H. This allowed us to explore the application of decay models with complexity beyond the simple sum of exponentials typically offered by commercially available deconvolution software.

Fitting was performed using Origin 2019 (OriginLab, Northampton MA, USA). A least-squares algorithm was used to vary the parameters of the fitting model until the χ_R^2 statistic was minimized. This was calculated using

$$\chi_R^2 = \frac{1}{n - l}\sum_{k=1}^{n}\frac{1}{\sigma_k^2}\left[I_{\mathrm{measured}}(t_k) - I_{\mathrm{model}}(t_k)\right]^2 \tag{4}$$

where n is the total number of time bins, l is the number of freely varying parameters in the model, and $I_{\mathrm{measured}}(t_k)$ and $I_{\mathrm{model}}(t_k)$ are the values of the fluorescence decay data and model at the time after excitation corresponding to bin k. σ_k is the expected standard deviation of the data point, here given by (24)

$$\sigma_k = \sqrt{I_{\parallel}(t_k) + 4I_{\perp}(t_k)} \tag{5}$$

Models of increasing complexity were attempted until the χ_R^2 statistic of the best fit was no longer improved by the addition of further components. The 95% parameter confidence intervals were output by Origin using the model-comparison (F-test) approach. The quality of the fit was also assessed by inspection of the histogram of weighted residuals x_k, calculated from

$$x_k = \frac{I_{\mathrm{measured}}(t_k) - I_{\mathrm{model}}(t_k)}{\sigma_k} \tag{6}$$

Histogram bin widths were chosen using the Freedman-Diaconis rule (25). Residuals were inspected for normal distribution about zero by calculating their arithmetic mean and visually comparing the histogram with a best-fit Gaussian. The lower count rates achievable with two-photon excitation resulted in systematically offset residuals, so a modified approach to the analysis of these measurements was necessary (see Appendix S1).

Composite fluorescence anisotropy decay models (e.g., Eq. 16) were fit using the same least-squares methods as for the single-photon fluorescence intensity decays, but with the lifetime (τ_i) and amplitude (α_i) values (see Eq. 10) fixed using the results of the fluorescence intensity decay fitting and the expected standard deviation in each time bin t_k becoming

$$\sigma_k = \frac{\sqrt{\left[I_{\parallel}(t_k) + 4I_{\perp}(t_k)\right]R(t_k)^2 - 2\left[I_{\parallel}(t_k) - 2I_{\perp}(t_k)\right]R(t_k) + I_{\parallel}(t_k) + I_{\perp}(t_k)}}{I(t_k)} \tag{7}$$

by propagating the $\sqrt{I_{\parallel}}$ and $\sqrt{I_{\perp}}$ uncertainties of the polarized fluorescence decays through Eq. 3 (24). Using both Eqs. 1 and 3 to eliminate $I_{\parallel}$ and $I_{\perp}$ leads to the greatly simplified expression (26)

$$\sigma_k = \sqrt{\frac{(1 - R(t_k))(1 + 2R(t_k))(2 + R(t_k))}{3I(t_k)}} \tag{8}$$

2PA polarization ratios

Average steady-state two-photon absorption (2PA) polarization ratios $\overline{\Omega}$ were determined by measuring the ratio of fluorescence intensities after circularly and linearly polarized excitation at constant incident power (23),

$$\overline{\Omega} = \frac{\langle I_{\mathrm{circ}}(t)\rangle}{\langle I_{\mathrm{lin}}(t)\rangle} \tag{9}$$

$\langle I_{\mathrm{circ}}(t)\rangle$ and $\langle I_{\mathrm{lin}}(t)\rangle$ were measured by setting the emission polarizer to the appropriate magic angle (54.7° and 35.3° to the vertical for linearly and circularly polarized excitation respectively) and recording fluorescence for 30 s. This was repeated five times for each excitation polarization, with the final $\overline{\Omega}$ value given by the ratio of average total photon counts.

RESULTS

NADH and NADPH in binding equilibrium with their corresponding enzymes exhibit highly heterogeneous and contrasting fluorescence decay dynamics

The increased intensity of NAD(P)H fluorescence upon enzyme binding was recognized in the pioneering work of Britton Chance (27), with a corresponding increase in fluorescence lifetime first quantified by Gregorio Weber and coworkers in 1970 (28). In subsequent studies, the reported lifetimes of NADH and NADPH have varied between 1 and 6 ns depending on the specific enzyme under analysis and the presence of accompanying substrate molecules (29–32). Drawing conclusions from these data to determine the molecular mechanisms leading to fluorescence lifetime changes has proved difficult, presumably due to the limitations of the measurement techniques then available. For example, closely spaced lifetimes in multiexponential decays may have been obscured by early frequency domain techniques and in flash-lamp-based photon counting methods with low ($\sim 10^2$ Hz) count rates (33). In recent years, time-resolved fluorescence techniques have seen significant advances, and numerous studies have utilized two-photon excitation with mode-locked ($\sim 10^8$ Hz) Ti:sapphire lasers. These techniques are not without their drawbacks, as utilizing the full mode-locked pulse train may introduce inaccuracies due to the incomplete recording of the total fluorescence decay, limited to the ~10-ns inter-pulse separation (34–36). Polarization artifacts may also be introduced by the high (>1) numerical aperture objectives used for two-photon excitation and fluorescence collection (37–39). To overcome such issues, we have employed low NA (0.1) excitation, 90° excitation-detection optics, and full fluorescence polarization analysis (22,23). Sample excitation was achieved using the frequency-doubled output of an OPA pumped by a 250-kHz regeneratively amplified Ti:sapphire laser. This permitted the simultaneous collection of fluorescence intensity and anisotropy decay data with 400-ns pulse-to-pulse separation at a maximum photon count rate of 2.5 kHz.

We performed polarization-resolved TCSPC on solutions of NADH and NADPH with lactate dehydrogenase and isocitrate dehydrogenase respectively. The total intensity decay data were fit to multiexponential functions of the form

$$I(t) = I(\infty) + I(0)\sum_{i=1}^{m}\alpha_i e^{-t/\tau_i} \tag{10}$$

where $I(\infty)$ accounts for any small contributions from time-uncorrelated background and α_i is the fractional amplitude of species i with lifetime τ_i. Best fit parameters are summarized in Table 1. Both solutions exhibited strongly heterogeneous fluorescence with three decay ($m = 3$) components required for an acceptable fit ($\chi_R^2 = 1.99$ for NADH and 1.85 for NADPH). Simpler decay functions gave poor fits, with asymmetrically distributed residuals and χ_R^2 values of 173.1 and 720.4 (mono-exponential) and 8.87 and 21.1 (bi-exponential), respectively (Fig. 2). The majority (77% and 85.9%) decay component in both solutions, with a lifetime of approximately 0.4 ns (τ_1), would correspond to free NADH or NADPH, in line with assignments in living cells (1). This is likely an average of the 0.3-ns and 0.7-ns decay components observed in aqueous solutions (22,40), suggested to correspond to *cis* and *trans* configurations of the amide group on the nicotinamide ring (23,41). An increase in the NAD(P)H fluorescence lifetime upon enzyme binding is well established (1). Here, introduction of an enzyme to solutions of NADH or NADPH resulted in the appearance of two longer (nanosecond) decay components of 1.34 and 1.59 ns (τ_2), and 3.2 and 4.4 ns (τ_3) respectively. In the next section, time-resolved fluorescence anisotropy measurements will

TABLE 1 Fluorescence intensity decay parameters of NADH in solution with lactate dehydrogenase and NADPH with isocitrate dehydrogenase, and in ternary complex with reduced substrates

	NADH + LDH	+Lactate	NADPH + IDH	+Isocitrate
τ_1/ns	0.43 [0.42, 0.44]	0.47 [0.46, 0.49]	0.403 [0.397, 0.409]	0.414 [0.406, 0.422]
τ_2/ns	1.34 [1.30, 1.37]	1.9 [1.8, 2.0]	1.59 [1.54, 1.64]	1.70 [1.63, 1.77]
τ_3/ns	3.2 [3.0, 3.4]	3.6 [3.5, 3.8]	4.4 [4.2, 4.5]	5.30 [5.2, 5.4]
α_1/%	77 [75, 78]	59 [58, 61]	85.9 [85.1, 86.7]	86 [85, 88]
α_2/%	22.5 [21.7, 23.5]	29 [28, 30]	12.3 [11.9, 12.7]	11.4 [10.9, 11.9]
α_3/%	0.9 [0.6, 1.1]	11 [10, 13]	1.8 [1.7, 2.0]	2.3 [2.2, 2.5]

Square brackets indicate 95% confidence intervals. IDH, isocitrate dehydrogenase; LDH, lactate dehydrogenase.

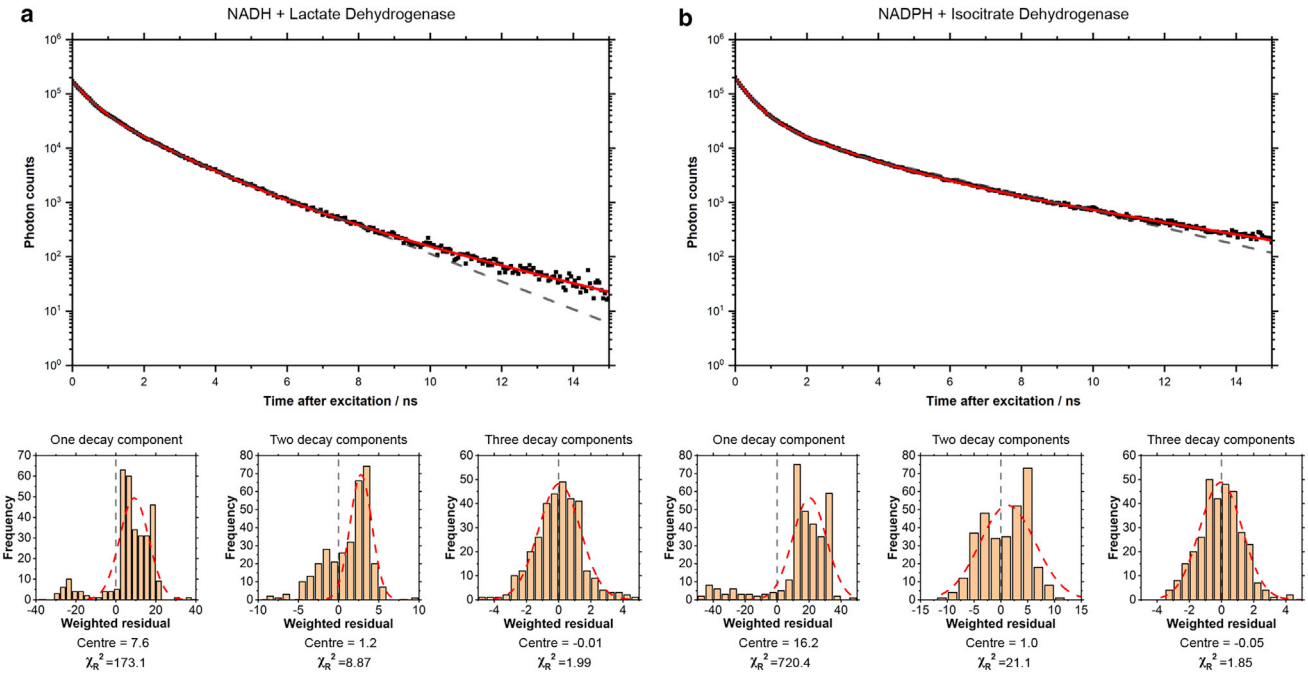

FIGURE 2 Fluorescence intensity decays of NADH or NADPH in solution with an enzyme contained three distinct decay components. Time-resolved intensity datasets were constructed using Eq. 1 and the polarized fluorescence decays shown in Figure S2. For both (*a*) NADH mixed with lactate dehydrogenase and (*b*) NADPH mixed with isocitrate dehydrogenase, simpler models with one and two decay components gave unevenly distributed, non-Gaussian residuals and high χ^2_R values. The poor fit of two-component models, particularly at excitation-emission delay times beyond 10 ns, is shown as a dotted gray line. To see this figure in color, go online.

be used to correlate each lifetime to the corresponding global and internal motions of the bound cofactors. Considering the longer lifetime of bound NADPH inside the cell (1,17), it was also interesting to note that both τ_2 and τ_3 were longer for bound NADPH than bound NADH in solution. For τ_2, the difference between NADH and NADPH was only 0.25 ns, whereas for τ_3 the increase was much larger at 1.2 ns. The relative proportion of τ_3 and τ_2 was also almost four times larger in NADPH bound to isocitrate dehydrogenase, with $\alpha_3/\alpha_2 = 0.15$ compared with 0.04 in NADH bound to lactate dehydrogenase. Although our prior 1.5 ($\pm$0.2) ns estimate of the lifetime of bound NADH in the cell agreed with the τ_2 species of NADH bound in solution, it was the τ_3 species of bound NADPH in solution that corresponded to the estimate of 4.4 ($\pm$0.2) ns for the lifetime of bound intracellular NADPH (17).

NADH and NADPH undertake their intracellular roles by donating hydride ions in the enzyme-catalyzed reduction of substrates. A number of previous studies have reported additional increases to the fluorescence lifetimes of bound NADH and NADPH when substrate molecules are simultaneously present in a ternary complex (28,30,31). To investigate the origins of these observations, we added a saturated solution of sodium lactate or sodium isocitrate into our enzyme and cofactor mixtures at the end of each initial experiment and undertook identical fluorescence decay measurements. As the products of the reactions catalyzed by the two enzymes when reduced cofactors are present, these substrates would occupy the binding site without causing oxidation to non-fluorescent NAD+ and NADP+ (42,43). The lifetimes of the two bound components were slightly longer in the ternary complex of NADH, lactate dehydrogenase and lactate, with τ_2 increasing from 1.34 to 1.9 ns and τ_3 increasing from 3.2 to 3.6 ns. More significant were the changes in the relative amplitudes of each decay component. Lactate was seen to drive the equilibrium toward the bound species, with α_1 decreasing from 77% to 59%. The relative abundance of the longer-lifetime bound species was also significantly higher, with the ratio α_3/α_2 increasing to 0.38 from 0.04. In contrast, we observed little change in the NADPH binding equilibrium induced by isocitrate and there was only a very minor increase in τ_2, from 1.59 to 1.70 ns. However, τ_3 increased substantially, from 4.4 to 5.3ns. Potential mechanisms governing the contrasting influences of lactate and isocitrate on the NADH and NADPH binding equilibria, alongside the differences in their bound lifetimes, are explored in the "discussion" section.

Time-resolved fluorescence anisotropy reveals two distinct binding configurations

Time-resolved fluorescence anisotropy measurements were used to investigate differences in the environment and orientational dynamics of the three fluorescent

populations observed in the intensity decays. The fluorescence anisotropy of such multi-component systems reports on the net transition dipole moment orientation of the excited state population (22,23). For a homogeneous emitting population in an isotropic solution, the time-dependent fluorescence anisotropy $R(t)$ is sensitive to the global and internal motions of the chromophore and decays monotonically to zero (24). However, for the solutions of both NADH and lactate dehydrogenase and NADPH and isocitrate dehydrogenase, we observed a clear departure from such dynamics with a pronounced dip and rise in $R(t)$ (Fig. 3 *a* and *b*). This phenomenon has previously been observed in a range of biological systems exhibiting heterogeneous fluorescence dynamics (32,44–47) and can be qualitatively interpreted by a comparison with the time-varying fractional contribution of each species to the overall fluorescence (Fig. 3 *c* and *d*). Before 1 ns, the short-lifetime τ_1 population predominates and the anisotropy decays rapidly, indicating this to be a rapidly depolarizing species. Beyond 2 ns, the preponderance of the emission arises from the τ_2 and τ_3 species and the net anisotropy returns to 80%–90% of its maximum value (0.4), thereafter decaying monotonically and slowly, reducing by approximately 0.05 over the next 10 ns. This indicates that these populations are undergoing significantly slower rotational diffusion. This is consistent with

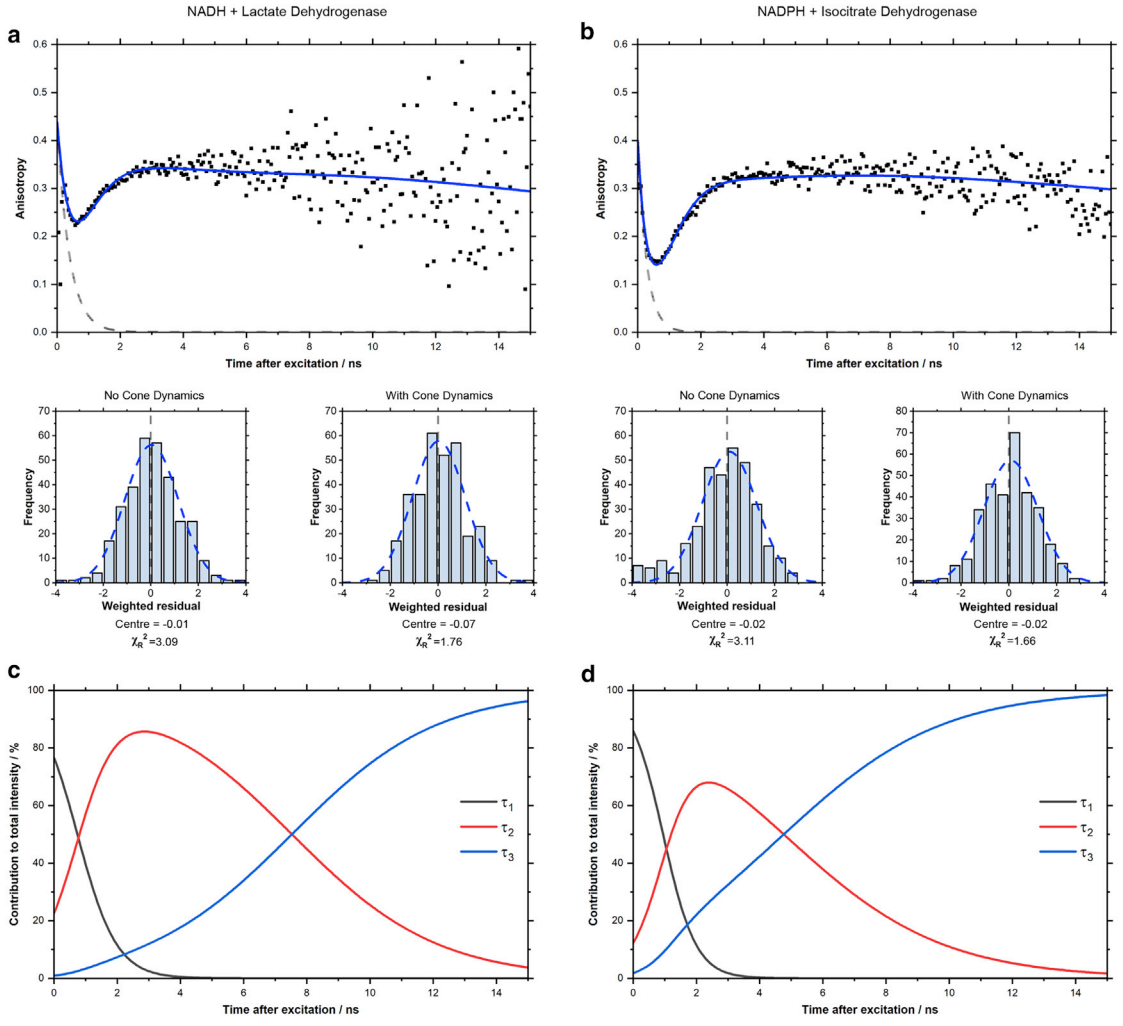

FIGURE 3 The dip-and-rise dynamics of the time-resolved fluorescence anisotropies revealed that both longer-lifetime components were associated with slow rotational correlation times. Time-resolved anisotropy datasets were constructed using Eq. 3 and the same polarized fluorescence decays as the time-resolved intensity measurements in Fig. 1 (see Fig. S2). For both (*a*) NADH with lactate dehydrogenase and (*b*) NADPH with isocitrate dehydrogenase, acceptable composite anisotropy fits required the introduction of dynamics described by the wobbling-in-a-cone model to the bound components (Eq. 13). These revealed that the shorter-lifetime enzyme-bound component (τ_2) possessed greater orientational freedom than the longer-lifetime species (τ_3) in both cofactors. The gray dotted lines in each decay correspond to the anisotropy decay of free NAD(P)H measured in our previous work (22). The time-varying fractional intensities of each component (*c* and *d*), calculated using Eq. 12 and the parameters in Table 1, provide fit-free indication that both τ_2 and τ_3 are enzyme-bound species, with these components dominating the signal from 2 ns onward and the anisotropy remaining high. To see this figure in color, go online.

Web 3C

the assignment of τ_1 to freely diffusing NAD(P)H and τ_2 and τ_3 line to enzyme-bound species.

Quantifying the observed depolarization dynamics involves fitting of an appropriate decay model to the anisotropy data. $R(t)$ is necessarily exponential for a homogeneous population of freely diffusing fluorophores (48). However, additional complexity will be introduced by the mixed populations of free and enzyme-bound cofactors studied here. For a heterogeneous population, the time evolution of the composite anisotropy is a sum of the individual anisotropy decays, each weighted by their time-varying fractional contribution to the overall fluorescence intensity $A_i(t)$ (49),

$$R(t) = \sum_{i=1}^{m} A_i(t) R_i(t) \tag{11}$$

$$A_i(t) = \frac{\alpha_i e^{-t/\tau_i}}{\sum_{j=1}^{m} \alpha_j e^{-t/\tau_j}} \tag{12}$$

In addition, although unbound NAD(P)H molecules will be expected to exhibit free diffusion, several X-ray diffraction studies have reported difficulties in resolving the nicotinamide moiety in the dehydrogenase-bound cofactor (50,51), implying it to be highly mobile (52,53). This has also been confirmed using nuclear magnetic resonance (NMR) spectroscopy (53). The diffusional motion of bound fluorophores is therefore likely to include contributions from both the global motion of the enzyme and the local motion of the cofactor itself (54). The time-resolved fluorescence anisotropy of such systems has been successfully described by the "wobbling-in-a-cone" model (24,55,56). This assigns a bi-exponential fluorescence anisotropy decay for each bound species,

$$R(t) = R(0)\left[B e^{-t/\tau_{\text{fast}}^{\text{rot}}} + (1 - B) e^{-t/\tau_{\text{slow}}^{\text{rot}}}\right] \tag{13}$$

The slower rotational correlation time $\tau_{\text{slow}}^{\text{rot}}$ results from the tumbling of the overall complex, whereas the faster time $\tau_{\text{fast}}^{\text{rot}}$ includes contributions from both the rates of tumbling and local diffusion. The fluorescence anisotropy immediately after excitation, $R(0)$, is determined by the angle between the absorption and emission transition dipoles and for single-photon excitation is 0.4 if these are collinear. The relative amplitudes of the two decay components relate to the angle of the cone swept out within the local motion ψ_c,

$$\cos\psi_c = \frac{-1 \pm \sqrt{1 + 8\sqrt{1 - B}}}{2} \tag{14}$$

Using this angle, the contribution of the overall tumbling to $\tau_{\text{fast}}^{\text{rot}}$ can be removed to reveal the diffusion coefficient of the motion within the cone, D_{cone}, (56)

$$D_{\text{cone}} = \frac{\left(1/\tau_{\text{fast}}^{\text{rot}}\right) - \left(1/\tau_{\text{slow}}^{\text{rot}}\right)}{B}\left[\left(\frac{1 - \cos\psi_c}{24}\right) \times \left(6 + 8\cos\psi_c - \cos^2\psi_c - 12\cos^3\psi_c - 7\cos^4\psi_c\right) - \frac{\cos^2\psi_c(1 + \cos\psi_c)^2}{2(1 - \cos\psi_c)} \times \left\{\ln\left(\frac{1 + \cos\psi_c}{2}\right) + \left(\frac{1 - \cos\psi_c}{2}\right)\right\}\right] \tag{15}$$

By assuming the slower rotational correlation time is shared between τ_2 and τ_3, as they result from binding to identical enzymes, the composite anisotropy decay (Eqs. 11 and 12) becomes

$$R(t) = \frac{R(0)}{\alpha_1 e^{-t/\tau_1} + \alpha_2 e^{-t/\tau_2} + \alpha_3 e^{-t/\tau_3}} \times \left(\alpha_1 e^{-t/\tau_1} e^{-t/\tau_{\text{free}}^{\text{rot}}} + \alpha_2 e^{-t/\tau_2}\left\{B_2 e^{-t/\tau_2^{\text{cone}}} + [1 - B_2] e^{-t/\tau_{\text{slow}}^{\text{rot}}}\right\} + \alpha_3 e^{-t/\tau_3}\left\{B_3 e^{-t/\tau_3^{\text{cone}}} + [1 - B_3] e^{-t/\tau_{\text{slow}}^{\text{rot}}}\right\}\right) \tag{16}$$

where unbound NAD(P)H undergoes unrestricted rotational diffusion with correlation time $\tau_{\text{free}}^{\text{rot}}$. This model gave good fits to the experimental data, with evenly distributed residuals and $\chi_R^2 = 1.76$ for NADH and lactate dehydrogenase and 1.66 for NADPH and isocitrate dehydrogenase. The fit parameters were also physically realistic, with the ratio of the global rotational correlation times ($\tau_{\text{slow}}^{\text{rot}}$) between the two enzymes equal to the ratio of their molecular weights, in agreement with the Stokes-Einstein-Debye equation (see Appendix S2). This was not the case for models in which the local NAD(P)H motion was not included (achieved by fixing both B_2 and B_3 at zero), which was also accompanied by an increase in the χ_R^2 values to 3.09 and 3.11 respectively. Moreover, introducing separate $R(0)$ values for each species gave no improvement in the fit quality.

In both mixtures, the parameters from fitting Eq. 16 revealed clearly differing local diffusive motion for the two enzyme-bound species (Table 2), returning $B_2 > B_3$ in all cases with well-separated confidence intervals. In NADH bound to lactate dehydrogenase, τ_2 corresponded to a binding state in which the cofactor was observed to diffuse within a cone angle of 20° at a rate of 0.03 ns^{-1}, over 10 times slower than the equivalent rate of free NADH diffusion $D_{\text{free}} = 1/6\tau_{\text{free}}^{\text{rot}} = 0.43$ ns^{-1}. In contrast, τ_3 was fully constrained, with $\psi_{\text{long}} = 0°$, albeit with a 95% confidence interval up to 8°. This absence of local motion effectively removes τ_3^{cone} from the model ($B_3 = 0$) and sets its diffusion coefficient to zero. For NADPH and isocitrate

TABLE 2 Measured (a) and derived (b) parameters describing the composite anisotropy decays of NADH with lactate dehydrogenase and NADPH with isocitrate dehydrogenase, and in ternary complexes

a	NADH + LDH	+Lactate	NADPH + IDH	+Isocitrate
$R(0)$	0.409 [0.399, 0.417]	0.41 [0.39, 0.43]	0.40 [0.39, 0.42]	0.40 [0.37, 0.43]
$\tau_{\text{free}}^{\text{rot}}$/ns	0.39 [0.38, 0.41]	0.18 [0.17, 0.21]	0.282 [0.281, 0.288]	0.27 [0.25, 0.29]
B_2	0.17 [0.15, 0.18]	0.30 [0.27, 0.35]	0.22 [0.21, 0.23]	0.32 [0.26, 0.43]
τ_2^{cone}/ns	1.1 [0.9, 1.3]	1.4 [1.2, 1.9]	0.09 [0.04, 0.13]	0.5 [0.2, 0.6]
B_3	0.00 [−0.11, 0.03]	0.02 [0, 0.04]	0.00 [−0.02, 0.01]	0.00 [−0.01, 0.03]
τ_3^{cone}/ns	–	–	–	–
$\tau_{\text{slow}}^{\text{rot}}$/ns	38 [35, 49]	45 [40, 51]	51 [48, 57]	26 [21, 29]
b	**NADH + LDH**	**+Lactate**	**NADPH + IDH**	**+Isocitrate**
D_{free}/ns^{-1}	0.43 [0.41, 0.44]	0.9 [0.8, 1.0]	0.591 [0.578, 0.592]	0.63 [0.58, 0.66]
D_{tumble}/ns^{-1}	0.0044 [0.0034, 0.0048]	0.0037 [0.0033, 0.0041]	0.0032 [0.0029, 0.0035]	0.006 [0.005, 0.008]
$\psi_{\text{bound}}^{\text{short}}$/°	20 [19, 21]	27 [26, 30]	23.3 [22.7, 23.9]	28 [25, 34]
$D_{\text{cone}}^{\text{short}}$/ns^{-1}	0.03 [0.02, 0.05]	0.04 [0.02, 0.08]	0.5 [0.3, 1.2]	0.1 [0.0, 0.7]
ψ_{long}/°	0 [−15, 8]	7 [−4, 8]	0 [−7, 5]	0 [−5, 7]

Square brackets indicate 95% confidence intervals.

dehydrogenase, no local motion was again observed for the longest-lifetime species. However, although the shorter-lifetime bound species (τ_2) exhibited a similar degree of confinement to that for NADH bound to lactate dehydrogenase ($\psi_{\text{bound}}^{\text{short}} = 23°$), they underwent a faster degree of local motion with $D_{\text{cone}}^{\text{short}} = 0.5$ ns^{-1}. This would indicate that the nicotinamide of the τ_2 population in NADPH, although constrained, appears to experience a greater exposure to the solvent. However, the corresponding rotational correlation time is close to the IRF of the TCSPC system, which likely introduces quantitative inaccuracies to this parameter value. The corresponding motion of the τ_2 population in NADH must experience a larger degree of local friction, implying a greater degree of incorporation of the nicotinamide moiety into the binding site.

After the addition of lactate, the time-resolved fluorescence anisotropy revealed that the only significant change in the diffusional characteristics of the nicotinamide moiety of bound NADH was a small (7°) increase in the cone angle of the τ_2 species (Table 2). Any simultaneous increase in the cone angle of the τ_3 species was obscured by its confidence interval overlapping with zero. A rise in $\psi_{\text{bound}}^{\text{short}}$ was also observed upon the addition of isocitrate to the NADPH mixture with a possible decrease in the associated diffusion coefficient, from 0.5 to 0.1 ns^{-1}, obscured, however, by the large uncertainty in the value for the binary complex. Interestingly, we also observed an increase in the diffusion coefficient of the overall tumbling motion of the isocitrate dehydrogenase ternary complex compared with the complex with NADPH alone, at 0.0032 ns^{-1} compared with 0.006 ns^{-1}. Given that isocitrate is unlikely to significantly alter the volume or shape of the enzyme complex, this may suggest that its addition alters the solvent-solute boundary conditions (22). However, an alternative explanation may be provided by the results of a *post hoc* computational investigation into the impact on the fitting parameters resulting from the exclusion of the IRF (Appendix S3). Although this confirmed that the contrasting restriction of the two bound states ($B_2 > B_3$) could indeed be successfully resolved using our approach, repeatedly re-generating Poisson noise on the simulated datasets resulted in a large spread in the returned values for $\tau_{\text{slow}}^{\text{rot}}$, ranging from 29 to 52 ns. This would result from the low fluorescence signal at extended delay times due to $\tau_{\text{slow}}^{\text{rot}} > \tau_3$ and suggests that significantly extended acquisition times would be required to investigate these observations in more detail.

Two-photon polarization ratios indicate two differing nicotinamide enzyme-binding geometries for both NADH and NADPH

In previous work, we demonstrated that the fluorescence lifetimes of NADH and NADPH are mediated through constraints to the conformational freedom of the nicotinamide ring, reducing the rate of non-radiative transition from the excited to ground state by activated barrier crossing (22). Such constriction should manifest as a decreased diffusion coefficient in time-resolved fluorescence anisotropy measurements. In the mixture of NADH and lactate dehydrogenase, the longer lifetime of the τ_2 bound species over that of the free species was indeed correlated with a smaller $D_{\text{cone}}^{\text{short}}$ than D_{free}. However, the equal diffusion rates of the τ_1 and τ_2 species in mixtures of NADPH and isocitrate dehydrogenase implied that the rate of activated barrier crossing was not reflected in the rate of local diffusional motion alone. We recently showed that changes in the fluorescence lifetimes of NADH and NADPH can also result from altered geometries of the nicotinamide ring, presumably through modifications to the barrier frequencies that control the non-radiative decay process (23). This was revealed by the polarization dependence of 2PA, measured by the ratio of absorption strengths with circularly and linearly

polarized two-photon excitation. This value, denoted Ω, reflects the symmetry of the two-photon transition (57). As this involves transfer of charge across the nicotinamide moiety in NADH and NADPH (2,4), altered values of Ω may imply changes in the nicotinamide geometry (23). We therefore performed polarized 2PA measurements on the NAD(P)H-enzyme solutions to investigate whether this was occurring in the bound populations.

Ω measurements are typically made by comparing the steady-state fluorescence intensity after circularly and linearly polarized two-photon excitation with equal incident power (58). In a heterogeneous mix of fluorophores, this will provide a population average (23) that we denote $\overline{\Omega}$ (see section "methods"). As the restricted two-photon excitation volume, localized to the beam waist of the excitation laser (59), leads to lower fluorescence intensities compared with single-photon fluorescence measurements, we carried out steady-state polarized 2PA measurements on new preparations in which we further concentrated the enzyme-bound population through repeated centrifugal filtration. From these, we measured $\overline{\Omega} = 1.04\ (\pm 0.01)$ for NADH with lactate dehydrogenase and $\overline{\Omega} = 0.94\ (\pm 0.01)$ for NADPH and isocitrate dehydrogenase. As we previously observed aqueous solutions of NADH and NADPH to exhibit $\overline{\Omega} = 0.8\ (\pm 0.1)$ (23), these results indicated that enzyme binding causes a change in the nicotinamide geometry in at least one of the species. The larger value for NADH and lactate dehydrogenase could have resulted from the presence of a larger proportion of enzyme-bound species relative to the NADPH and isocitrate dehydrogenase mixtures or may have reflected a fundamental difference in the individual Ω values of the τ_2 and τ_3 species in NADH and NADPH. Determination of the component Ω parameters required time-resolved two-photon fluorescence measurements using linearly and circularly polarized excitation. The polarization ratio for each component is then given by (23)

$$\Omega_i = \frac{\alpha_i^{\mathrm{circ}} \sum_{i=1}^{3} \alpha_i^{\mathrm{lin}} \tau_i^{\mathrm{lin}}}{\alpha_i^{\mathrm{lin}} \sum_{i=1}^{3} \alpha_i^{\mathrm{circ}} \tau_i^{\mathrm{circ}}} \overline{\Omega} = \frac{\alpha_i^{\mathrm{circ}} \langle \tau_{\mathrm{lin}} \rangle}{\alpha_i^{\mathrm{lin}} \langle \tau_{\mathrm{circ}} \rangle} \overline{\Omega} \qquad (17)$$

Our two-photon fluorescence decay measurements unavoidably contained an order of magnitude fewer photons than with single-photon excitation. This required us to adopt a maximum likelihood fitting approach (see section "methods" and Appendix S1). We sought to minimize the accompanying drop in precision by reducing the number of freely varying parameters. From Kasha's rule (60), as both linearly and circularly polarized excitation would result in emission from the lowest energy excited state, the lifetimes of the three species would be expected to be equal in the two fluorescence decays. We therefore performed global fits in which the lifetimes τ_1, τ_2, and τ_3 were shared between both datasets. This decreased uncertainties in the lifetimes by a factor of two. However, the individual lifetimes remained relatively imprecise compared with the single-photon measurements, with average uncertainties of 50% (see Table S1). Fortunately, the separate Ω values of each decay component depend on the overall amplitude-weighted mean lifetime of the sample (Eq. 17) to account for changes in the average quantum yield of the mixtures with each excitation mode (23). The uncertainties in this composite parameter were more reasonable (10%–20%). Furthermore, the precision of the relative decay amplitudes of each component was sufficiently high to reveal clear differences between circularly and linearly polarized excitation. In NADH and lactate dehydrogenase, the amplitudes of the τ_1 and τ_3 components were larger with linearly polarized excitation, at $\alpha_1^{\mathrm{lin}} = 21(\pm 1)\%$ compared to $\alpha_1^{\mathrm{circ}} = 9(\pm 1)\%$ and $\alpha_3^{\mathrm{lin}} = 10(\pm 2)\%$ compared to $\alpha_3^{\mathrm{circ}} = 4(\pm 5)\%$. In contrast, the amplitude of the τ_2 component was larger for circularly polarized excitation, with $\alpha_2^{\mathrm{circ}} = 87(\pm 4)\%$ and $\alpha_2^{\mathrm{lin}} = 69(\pm 1)\%$. This pattern of relative amplitudes was also observed for NADPH with isocitrate dehydrogenase.

Table 3 shows the clearly distinct Ω values calculated for the two bound NADH species, with $\Omega_2 = 1.3\ (\pm 0.2)$ and $\Omega_3 = 0.4\ (\pm 0.4)$. Similar results were also found for NADPH, with $\Omega_2 = 1.2\ (\pm 0.1)$ and $\Omega_3 = 0.6\ (\pm 0.4)$. The 0.3- and 0.7-ns single-photon excited lifetimes present in aqueous NAD(P)H solutions were again represented by a single short lifetime component in these measurements, with corresponding Ω_1 values of 0.4 (± 0.1) and 0.63 (± 0.08) for NADH and NADPH respectively. Our earlier work revealed that the two free species exhibit Ω values of 0.6 (± 0.1) and 1.1 (± 0.2), likely reflecting distinct values for the *cis* and *trans* geometries of the amide group of the nicotinamide (23). The lower Ω values here might result from the experimental conditions pushing the equilibrium of the unbound cofactors toward one of the two forms, perhaps due to the preference of binding sites for the *trans* configuration (23,61). However, these small values are more likely an artifact of the low signal levels from the τ_1 population. Only 3% of the photons counted from the NADH and lactate dehydrogenase measurements were emitted from this species ($\alpha_1\tau_1/\sum \alpha_i\tau_i$). This increased to 20% in the NADPH and isocitrate dehydrogenase mixtures, where Ω_1 was closer to our previously obtained values.

TABLE 3 Polarized two-photon absorption ratios Ω calculated for each species of NADH mixed with lactate dehydrogenase and NADPH mixed with isocitrate dehydrogenase, and in ternary complexes

	NADH + LDH	+Lactate	NADPH + IDH	+Isocitrate
Ω_1	0.4 (±0.1)	0.4 (±0.2)	0.63 (±0.08)	0.27 (±0.04)
Ω_2	1.3 (±0.2)	1.42 (±0.09)	1.2 (±0.1)	1.3 (±0.2)
Ω_3	0.4 (±0.4)	0.82 (±0.05)	0.6 (±0.4)	0.5 (±0.4)

Ω_2 values that exceed those measured from free NADH and NADPH confirmed an altered nicotinamide geometry in the shorter-lifetime bound species and hence may explain the increased lifetime of the τ_2 component in NADPH bound to isocitrate dehydrogenase relative to τ_1 even with equal diffusion coefficients. To within experimental accuracy, we found that the addition of substrate altered the 2PA polarization ratio Ω only in the τ_3 population of NADH bound to lactate dehydrogenase, increasing to 0.82 ($\pm$0.05) from 0.4 ($\pm$0.4). We also note that all Ω values were within the theoretical limits of 0.25–1.5 for the planar two-photon transition in NAD(P)H (4,58), providing additional confidence in these measurements.

DISCUSSION

We have observed two distinct fluorescence lifetimes arising from the binding of NADH and NADPH to lactate dehydrogenase and isocitrate dehydrogenase respectively. For each enzyme, these correspond to two different configurations. The shorter lifetime (τ_2) is associated with binding in which the cofactor is free to move within a cone angle of approximately 20°. As spontaneous emission in NADH and NADPH involves the nicotinamide moiety, the cofactors in this state must be bound at the opposing adenine/phosphate end. This conclusion is reinforced by circular dichroism studies that show a lower Michaelis constant associated with binding of the adenine moiety than the nicotinamide (62), reflected by our results with $\alpha_2 > \alpha_3$ in all mixtures. Eliminating local nicotinamide motion upon its binding then produces the longer-lifetime (τ_3) bound species (Fig. 4). Local nicotinamide motion in the bound state has previously been recognized in time-resolved anisotropy measurements on NAD(P)H autofluorescence in living tissues (32). Here we took advantage of the extended collection times achievable when studying bound NADH and NADPH in solution, alongside recording of the complete polarized fluorescence decay, to apply composite wobbling-in-a-cone anisotropy models to quantify the distinct binding configurations and identify the fluorescence lifetimes associated with each for the first time.

As inside cells (17), the fluorescence lifetimes associated with NADPH binding in solution were longer than for the corresponding species in bound NADH. This can be understood through the extensive efforts made to study differences in the NADH and NADPH binding sites to facilitate the creation of novel enzymes with the cofactor specificity switched (50,63–65). These are desirable for industrial biotechnology where the use of NADH, rather than NADPH, would be preferable due to its higher stability and lower production cost (3). X-ray diffraction studies have demonstrated that electrostatic effects are the principal means by which binding sites differentiate between the two

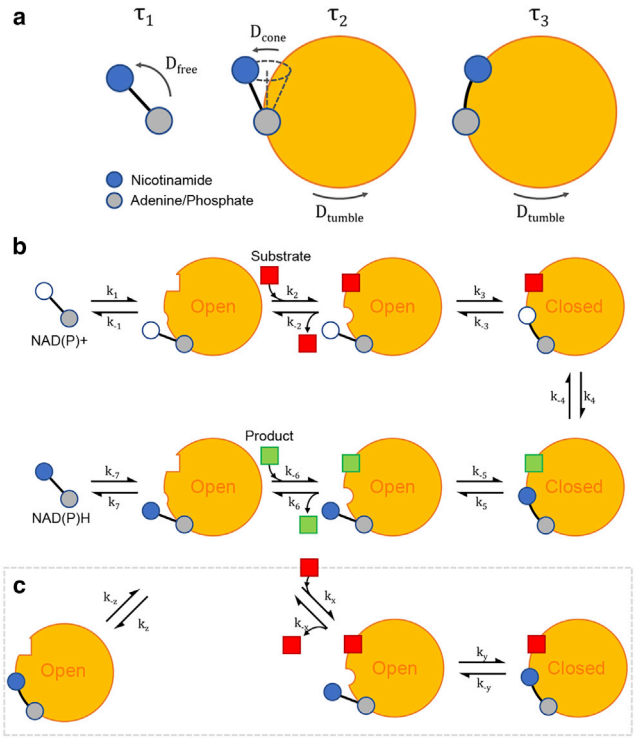

FIGURE 4 Conformational heterogeneity in the dehydrogenase reaction mechanism. (*a*) In solutions of NADH or NADPH with a corresponding enzyme, the shortest-lifetime species (τ_1) exhibited rapid rotational diffusion, the intermediate-lifetime species (τ_2) displayed rotational diffusion consistent with a cone model, and the longest-lifetime species (τ_3) was associated with only the slow tumbling of the enzyme. (*b*) These configurations participate in the reaction mechanism of a dehydrogenase, in which the open τ_2 form promotes the binding of substrate and the closed τ_3 form facilitates hydride transfer. (*c*) Catalytically unproductive, abortive conformations are also possible, such as when reduced substrate binds alongside reduced cofactors. To see this figure in color, go online.

cofactors (3). NADH binding sites contain negatively charged amino acids that form hydrogen bonds with the adenine ribose and cause repulsive forces toward the negatively charged phosphate group of NADPH. These are replaced by positively charged residues to confer specificity for NADPH and, importantly for the different fluorescence decay dynamics, result in a more rigid binding site (64). This would induce a longer fluorescence lifetime for NADPH by increasing conformational restriction and decreasing non-radiative relaxation (22,66). Supplementary mechanisms could nevertheless contribute; the nicotinamide moieties of NADH and NADPH may be constrained in different configurations (64) or be in direct contact with contrasting active site residues (63). Such contributions are indeed supported by our polarized two-photon absorption measurements on NADPH, where binding-induced alterations to the nicotinamide ring structure were resolved even in the absence of constraints to its diffusional motion. Such ring perturbations are known to facilitate hydride transfer in the active site (67).

Given our earlier predictions of 1.5 (±0.2) and 4.4 (±0.2) ns for the fluorescence lifetimes of enzyme-bound NADH and NADPH inside cells (17), our results suggest that intracellular NADPH is more likely to be found in the fully bound τ_3 state, whereas intracellular NADH is bound more loosely in the τ_2 state. To understand how this could occur, we must consider how the two binding configurations relate to the reaction mechanism of the enzymes and how these may differ inside the cell for NAD- and NADP-associated pathways. In general, enzymes must both sufficiently immobilize the reactants within the protein for catalysis but expose the binding sites to the surroundings for unimpeded ligand capture and release (68). Dehydrogenases overcome this apparent paradox by utilizing a structural change, transitioning between an open conformation, which allows substrate and cofactor binding and release, and a closed conformation, which facilitates the hydride transfer between the two (52,69). These conformations have been observed in structures of a wide range of enzymes, including isocitrate (70), glycerol 3-phosphate (71), glutamate (72), homoserine (73), malate (74), and alcohol (75) dehydrogenase. The reaction mechanism itself has been studied in most detail using lactate dehydrogenase as a model system (52,68,76). This has revealed that the adenine end of the cofactor must bind first. Subsequent binding of the substrate then initiates structural rearrangements that promote both the attachment of the nicotinamide and the open-to-closed transition of the ligand binding pocket, bringing the reactants close enough for hydride transfer. The process then occurs in reverse to reopen the binding pocket and release the product and cofactor.

In our experiments, the conformational freedom of the nicotinamide identified in the short-lifetime bound population (τ_2) suggests this corresponds to NAD(P)H bound to the open-conformation enzyme. The complete restriction of local nicotinamide motion in the long-lifetime bound species (τ_3) suggests this to be NAD(P)H bound to the enzyme in its closed conformation. The presence of this species even in the absence of substrate is in agreement with the work of Qiu et al., who observed the open and closed forms in fast equilibrium under these conditions (68). The substrate-induced nature of the open-to-closed transition was also evident in our measurements by the 10-fold increase of α_3/α_2 upon the introduction of lactate to NADH with lactate dehydrogenase. This may clarify recent work by Ranjit et al. in which the fluorescence decay of NADH bound to lactate dehydrogenase was measured to be mono-exponential with a lifetime of 3.4 ns (77). To optimize the accuracy of their lifetime measurements, the authors eliminated free cofactors by lowering the dissociation constant using high concentrations of oxalate. This will also have promoted the closed enzyme conformation, resulting in a single lifetime close to the 3.6 ns we measured as τ_3 in the presence of substrate. The small difference could be attributable to a persisting minority of open-conformation enzymes that could not be resolved with the phasor method of fluorescence decay analysis. Only a 14% contribution from this species would be required if the single lifetime were an amplitude-weighted average of the substrate-associated τ_2 and τ_3 values that we observed.

In contrast to lactate dehydrogenase, isocitrate had no significant effect on the relative population of long- and short-lifetime bound species of NADPH and isocitrate dehydrogenase. The catalytic function of this enzyme is known to require a divalent metal ion to bind alongside the substrate to lower the activation energy by altering the redox potential of the reactants (78). Although these were absent from our solutions, the increase in the fluorescence lifetimes of each bound NADPH species upon isocitrate addition demonstrated that the substrate could nevertheless bind. The lack of a subsequent increase in α_3/α_2 implies a role for this ion in facilitating the transition between open and closed states. This is in agreement with structural studies in which the fully closed form could only be achieved with the metal ion present alongside substrate and cofactor (70).

To unite this model of dehydrogenase function with our knowledge of the time-resolved fluorescence of intracellular NADH and NADPH, we integrated our new understanding of their bound photophysics with a quantitative analysis of the reaction mechanism (see Appendix S4). This revealed two possible biochemical contributors to the longer lifetime of bound NADPH, relative to bound NADH, inside cells. The first involved an increased ratio of product binding to unbinding (k_{-6}/k_6 in Fig. 4) for NADPH-associated dehydrogenases in the complex cellular environment. Such a difference could facilitate the contrasting roles of the two cofactors; a higher k_{-6}/k_6 ratio would favor the recruitment of substrates for reduction in NADPH-associated anabolic reactions, whereas a lower value would promote the release of the products of NADH-associated catabolic oxidations. However, this model relies upon the fluorescence lifetime of the reduced cofactor being the same in ternary complex with oxidized products (pyruvate, α-ketoglutarate) as with the reduced substrates (lactate, isocitrate) measured here. There is evidence that oxidized substrates can provide an additional excited state decay route for the reduced cofactor through photoinduced electron transfer (79), decreasing the fluorescence lifetime. Under these circumstances, a second contributor to the longer fluorescence lifetime of bound NADPH inside cells would be the characteristic lower NADP+ to NADPH ratio promoting the formation of "abortive" complexes of the reduced cofactor alongside the reduced substrate (42,43). To determine which of these mechanisms has the greater influence on the contrasting intracellular fluorescence lifetimes of NADH and NADPH, further experiments will be required to quantify both the reaction rates of their associated enzymes and their excited-state dynamics in ternary complex with oxidized substrates.

CONCLUSIONS

This work has established, for the first time, links between the time-resolved fluorescence of NADH and NADPH and the reaction mechanisms of the enzymes to which they bind. This will allow the interpretation of intracellular NAD(P)H FLIM measurements in greater biochemical detail in terms of the equilibria between different enzyme conformations and the cofactor redox balances that drive them. We have also demonstrated the sensitivity of the time-resolved anisotropy to conformational changes involved in the dehydrogenase reaction mechanism, which will be important for understanding polarization-resolved NAD(P)H fluorescence inside cells as this imaging technique becomes more widespread (32,38). Moreover, our work highlights the importance of recognizing heterogeneity in biological fluorescence measurements to ensure key phenomena are not overlooked. Although fluorescence has played a major role in the study of biological processes due to its molecular-level sensitivity, adaptability to most classes of intracellular molecules, and applicability in intact complex tissues and whole organisms under physiological conditions (80), the drive toward quantitative descriptions of living systems will place a greater burden on understanding probe photophysics to obtain accurate, precise, and artifact-free results (81). The extensive heterogeneity of fluorescent populations in biological systems will therefore present a significant challenge (82). Characterizing the multiple states with distinct lifetimes exhibited both intrinsically by autofluorescent biochemical molecules and by otherwise homogeneous synthetic probes within heterogeneous biological environments will be facilitated by the ongoing application of the tools and methodologies we have advanced in this work.

SUPPORTING MATERIAL

Supporting material can be found online at https://doi.org/10.1016/j.bpj.2023.02.014.

AUTHOR CONTRIBUTIONS

T.S.B. and A.J.B. designed the experiments. T.S.B. carried out the experiments and analyzed the data. All authors drafted the manuscript.

ACKNOWLEDGMENTS

This work was supported by BBSRC grant "New approaches to studying redox metabolism using time-resolved NAD(P)H fluorescence and anisotropy" (BB/P018726/1) to A.J.B., M.R.D., and T.S.B., and BBSRC Discovery Fellowship "Autofluorescence across scales: an integrated understanding of redox cofactors as intrinsic probes of metabolic state" (BB/W009242/1) to T.S.B.

DECLARATION OF INTERESTS

The authors declare no competing interests.

REFERENCES

1. Blacker, T. S., and M. R. Duchen. 2016. Investigating mitochondrial redox state using NADH and NADPH autofluorescence. *Free Radic. Biol. Med.* 100:53–65.
2. De Ruyck, J., M. Famerée, …, D. Jacquemin. 2007. Towards the understanding of the absorption spectra of NAD(P)H/NAD(P)+ as a common indicator of dehydrogenase enzymatic activity. *Chem. Phys. Lett.* 450:119–122.
3. Chánique, A. M., and L. P. Parra. 2018. Protein engineering for nicotinamide coenzyme specificity in oxidoreductases: attempts and challenges. *Front. Microbiol.* 9:194.
4. Kierdaszuk, B., H. Malak, …, J. R. Lakowicz. 1996. Fluorescence of reduced nicotinamides using one- and two-photon excitation. *Biophys. Chem.* 62:1–13.
5. Mayevsky, A., and B. Chance. 2007. Oxidation-reduction states of NADH in vivo: from animals to clinical use. *Mitochondrion.* 7:330–339.
6. Chance, B., P. Cohen, …, B. Schoener. 1962. Intracellular Oxidation-reduction states in vivo. *Science.* 137:499–508.
7. Gaude, E., C. Schmidt, …, C. Frezza. 2018. NADH shuttling couples cytosolic reductive carboxylation of glutamine with glycolysis in cells with mitochondrial dysfunction. *Mol. Cell.* 69:581–593.e7.
8. Thomas, L. W., C. Esposito, …, M. Ashcroft. 2019. CHCHD4 regulates tumour proliferation and EMT-related phenotypes, through respiratory chain-mediated metabolism. *Cancer Metabol.* 7:7.
9. Becker, W. 2012. Fluorescence lifetime imaging - techniques and applications. *J. Microsc. (Oxf.).* 247:119–136.
10. Skala, M. C., K. M. Riching, …, N. Ramanujam. 2007. In vivo multiphoton fluorescence lifetime imaging of protein-bound and free nicotinamide adenine dinucleotide in normal and precancerous epithelia. *J. Biomed. Opt.* 12:024014.
11. Barkauskas, D. S., G. Medley, …, M. S. Roberts. 2020. Using in vivo multiphoton fluorescence lifetime imaging to unravel disease-specific changes in the liver redox state. *Methods Appl. Fluoresc.* 8:034003.
12. Lukina, M. M., L. E. Shimolina, …, M. V. Shirmanova. 2019. Interrogation of tumor metabolism in tissue samples ex vivo using fluorescence lifetime imaging of NAD(P)H. *Methods Appl. Fluoresc.* 8:014002.
13. Chacko, J. V., and K. W. Eliceiri. 2019. NAD(P)H fluorescence lifetime measurements in fixed biological tissues. *Methods Appl. Fluoresc.* 7:044005.
14. Cao, R., H. Wallrabe, …, A. Periasamy. 2020. Optimization of FLIM imaging, fitting and analysis for auto-fluorescent NAD(P)H and FAD in cells and tissues. *Methods Appl. Fluoresc.* 8:024001.
15. König, K. 2020. Review: clinical in vivo multiphoton FLIM tomography. *Methods Appl. Fluoresc.* 8:034002.
16. Deberardinis, R. J., and C. B. Thompson. 2012. Cellular metabolism and disease: what do metabolic outliers teach us? *Cell.* 148:1132–1144.
17. Blacker, T. S., Z. F. Mann, …, M. R. Duchen. 2014. Separating NADH and NADPH fluorescence in live cells and tissues using FLIM. *Nat. Commun.* 5:3936.
18. Majumder, P., T. S. Blacker, …, J. E. Gale. 2019. Multiphoton NAD(P)H FLIM reveals metabolic changes in individual cell types of the intact cochlea upon sensorineural hearing loss. *Sci. Rep.* 9:18907–18910.
19. Tosatto, A., R. Sommaggio, …, C. Mammucari. 2016. The mitochondrial calcium uniporter regulates breast cancer progression via HIF -1α. *EMBO Mol. Med.* 8:569–585.
20. Nickel, A. G., A. Von Hardenberg, …, C. Maack. 2015. Reversal of mitochondrial transhydrogenase causes oxidative stress in heart failure. *Cell Metabol.* 22:472–484.
21. Haythorne, E., M. Rohm, …, F. M. Ashcroft. 2019. Diabetes causes marked inhibition of mitochondrial metabolism in pancreatic β-cells. *Nat. Commun.* 10:2474.

22. Blacker, T. S., R. J. Marsh, …, A. J. Bain. 2013. Activated barrier crossing dynamics in the non-radiative decay of NADH and NADPH. *Chem. Phys.* 422:184–194.

23. Blacker, T. S., N. Nicolaou, …, A. J. Bain. 2019. Polarized two-photon absorption and heterogeneous fluorescence dynamics in NAD(P)H. *J. Phys. Chem. B.* 123:4705–4717.

24. Blacker, T. S., W. Chen, …, A. J. Bain. 2017. Investigating state restriction in fluorescent protein FRET using time-resolved fluorescence and anisotropy. *J. Phys. Chem. C Nanomater. Interfaces.* 121:1507–1514.

25. Zhukov, M., and A. Popov. 2014. Bin number selection for equidistant mutual information estimaton. *In* IEEE 34th International Scientific Conference on Electronics and Nanotechnology, ELNANO 2014 Conference Proceedings, pp. 259–263.

26. Lidke, K. A., B. Rieger, …, T. M. Jovin. 2005. The role of photon statistics in fluorescence anisotropy imaging. *IEEE Trans. Image Process.* 14:1237–1245.

27. Chance, B., and H. Baltscheffsky. 1958. Respiratory enzymes in oxidative phosphorylation. VII. Binding of intramitochondrial reduced pyridine nucleotide. *J. Biol. Chem.* 233:736–739.

28. Scott, T. G., R. D. Spencer, …, G. Weber. 1970. Emission properties of NADH. Studies of fluorescence lifetimes and quantum efficiencies of NADH, AcPyADH, and simplified synthetic models. *J. Am. Chem. Soc.* 92:687–695.

29. Yu, Q., and A. A. Heikal. 2009. Two-photon autofluorescence dynamics imaging reveals sensitivity of intracellular NADH concentration and conformation to cell physiology at the single-cell level. *J. Photochem. Photobiol., B.* 95:46–57.

30. Brochon, J. C., P. H. Wahl, …, M. Iwatsubo. 1976. Pulse fluorimetry study of beef liver glutamate dehydrogenase-reduced nicotinamide adenine dinucleotide phosphate complexes. *Biochemistry.* 15:3259–3265.

31. Gafni, A., and L. Brand. 1976. Fluorescence decay studies of reduced nicotinamide adenine dinucleotide in solution and bound to liver alcohol dehydrogenase. *Biochemistry.* 15:3165–3171.

32. Vishwasrao, H. D., A. A. Heikal, …, W. W. Webb. 2005. Conformational dependence of intracellular NADH on metabolic state revealed by associated fluorescence anisotropy. *J. Biol. Chem.* 280:25119–25126.

33. Lakowicz, J. R. 1999. Topics in Fluorescence Spectroscopy, Volume 1: Techniques. Springer.

34. Gorbunova, I. A., M. E. Sasin, …, O. S. Vasyutinskii. 2021. Two-photon excited fluorescence dynamics in enzyme-bound NADH: the heterogeneity of fluorescence decay times and anisotropic relaxation. *J. Phys. Chem. B.* 125:9692–9707.

35. Leung, R. W. K., S.-C. A. Yeh, and Q. Fang. 2011. Effects of incomplete decay in fluorescence lifetime estimation. *Biomed. Opt Express.* 2:2517–2531.

36. Sakai, Y., and S. Hirayama. 1988. A fast deconvolution method to analyze fluorescence decays when the excitation pulse repetition period is less than the decay times. *J. Lumin.* 39:145–151.

37. Fisz, J. J. 2007. Another look at magic-angle-detected fluorescence and emission anisotropy decays in fluorescence microscopy. *J. Phys. Chem. A.* 111:12867–12870.

38. Cong, A. T. Q., R. M. L. Pimenta, …, A. A. Heikal. 2021. Associated anisotropy of intrinsic NAD(P)H for monitoring changes in the metabolic activities of breast cancer cells (4T1) in three-dimensional collagen matrix. *Phys. Chem. Chem. Phys.* 23:12692–12705.

39. Devauges, V., C. Marquer, …, S. Lévêque-Fort. 2012. Homodimerization of amyloid precursor protein at the plasma membrane: a homo-FRET study by time-resolved fluorescence anisotropy imaging. *PLoS One.* 7:e44434.

40. Visser, A. J. W. G., and A. v. Hoek. 1981. The fluorescence decay of reduced nicotinamides in aqueous solution after excitation with a UV-mode locked Ar ion laser. *Photochem. Photobiol.* 33:35–40.

41. Gorbunova, I. A., M. E. Sasin, …, O. S. Vasyutinskii. 2020. Two-photon excited fluorescence dynamics in NADH in water-methanol solutions: the role of conformation states. *J. Phys. Chem. B.* 124:10682–10697.

42. Fromm, H. 1963. Determination of dissociation constants of coenzymes and abortive. *J. Biol. Chem.* 238:2938–2944.

43. Eggert, M. W., M. E. Byrne, and R. P. Chambers. 2011. Impact of high pyruvate concentration on kinetics of rabbit muscle lactate dehydrogenase. *Appl. Biochem. Biotechnol.* 165:676–686.

44. Steinmark, I. E., P. H. Chung, …, K. Suhling. 2020. Time-resolved fluorescence anisotropy of a molecular rotor resolves microscopic viscosity parameters in complex environments. *Small.* 16:1907139.

45. Smith, T. A., and K. P. Ghiggino. 2015. A review of the analysis of complex time-resolved fluorescence anisotropy data. *Methods Appl. Fluoresc.* 3:022001.

46. Jha, A., J. B. Udgaonkar, and G. Krishnamoorthy. 2009. Characterization of the heterogeneity and specificity of interpolypeptide interactions in amyloid protofibrils by measurement of site-specific fluorescence anisotropy decay kinetics. *J. Mol. Biol.* 393:735–752.

47. Chib, R., S. Raut, …, I. Gryczynski. 2014. Associated anisotropy decays of Ethidium Bromide interacting with DNA. *Methods Appl. Fluoresc.* 2:015003.

48. Wahl, P. 1979. Analysis of fluorescence anisotropy decays by a least square method. *Biophys. Chem.* 10:91–104.

49. Ludescher, R. D., L. Peting, …, B. Hudson. 1987. Time-resolved fluorescence anisotropy for systems with lifetime and dynamic heterogeneity. *Biophys. Chem.* 28:59–75.

50. Hurley, J. H., R. Chen, and A. M. Dean. 1996. Determinants of cofactor specificity in isocitrate dehydrogenase: structure of an engineered NADP+ → NAD+ specificity-reversal mutant. *Biochemistry.* 35:5670–5678.

51. Hurley, J. H., A. M. Dean, …, R. M. Stroud. 1991. Catalytic mechanism of NADP+-Dependent isocitrate dehydrogenase: implications from the structures of magnesium-isocitrate and NADP+ complexes. *Biochemistry.* 30:8671–8678.

52. Deng, H., N. Zhadin, and R. Callender. 2001. Dynamics of protein ligand binding on multiple time scales: NADH binding to lactate dehydrogenase. *Biochemistry.* 40:3767–3773.

53. Hammen, P. K., A. Allali-Hassani, …, H. Weiner. 2002. Multiple conformations of NAD and NADH when bound to human cytosolic and mitochondrial aldehyde dehydrogenase. *Biochemistry.* 41:7156–7168.

54. Ko, C. W., Z. Wei, …, L. Ying. 2009. Probing nanosecond motions of plasminogen activator inhibitor-1 by time-resolved fluorescence anisotropy. *Mol. Biosyst.* 5:1025–1031.

55. Kinosita, K., A. Ikegami, and S. Kawato. 1982. On the wobbling-in-cone analysis of fluorescence anisotropy decay. *Biophys. J.* 37:461–464.

56. Lipari, G., and A. Szabo. 1980. Effect of librational motion on fluorescence depolarization and nuclear magnetic resonance relaxation in macromolecules and membranes. *Biophys. J.* 30:489–506.

57. Drucker, R. P., and W. M. McClain. 1974. Polarized two-photon studies of biphenyl and several derivatives. *J. Chem. Phys.* 61:2609–2615.

58. Bain, A. J. 2015. Multiphoton processes. *In* Photonics: Scientific Foundations, Technology and Applications Wiley, pp. 279–320.

59. Larijani, B., and A. Bain. 2007. Biological applications of single- and two-photon fluorescence. *In* Chemical Biology: Applications and Techniques Wiley, pp. 163–197.

60. Del Valle, J. C., and J. Catalán. 2019. Kasha's rule: a reappraisal. *Phys. Chem. Chem. Phys.* 21:10061–10069.

61. Wu, Y. D., and K. N. Houk. 1993. Theoretical study of conformational features of NAD+ and NADH analogs: protonated nicotinamide and 1,4-dihydronicotinamide. *J. Org. Chem.* 58:2043–2045.

62. Delabar, J. M., S. R. Martin, and P. M. Bayley. 1982. The binding of NADH and NADPH to bovine-liver glutamate dehydrogenase: spectroscopic characterisation. *Eur. J. Biochem.* 127:367–374.

63. Kalinina, O. V., and M. S. Gelfand. 2006. Amino acid residues that determine functional specificity of NADP- and NAD-dependent isocitrate and isopropylmalate dehydrogenases. *Proteins.* 64:1001–1009.

64. Mittl, P. R., A. Berry, …, G. E. Schulz. 1994. Anatomy of an engineered NAD-binding site. *Protein Sci.* 3:1504–1514.

65. Scrutton, N. S., A. Berry, and R. N. Perham. 1990. Redesign of the coenzyme specificity of a dehydrogenase by protein engineering. *Nature.* 343:38–43.

66. Chen, Y. Q., J. Van Beek, …, R. Callender. 2002. Vibrational structure of NAD(P) cofactors bound to three NAD(P) dependent enzymes: an investigation of ground state activation. *J. Phys. Chem. B.* 106:10733–10740.

67. Beis, K., S. T. M. Allard, …, J. H. Naismith. 2003. The structure of NADH in the enzyme dTDP-D-glucose dehydratase (RmlB). *J. Am. Chem. Soc.* 125:11872–11878.

68. Qiu, L., M. Gulotta, and R. Callender. 2007. Lactate dehydrogenase undergoes a substantial structural change to bind its substrate. *Biophys. J.* 93:1677–1686.

69. Suzuki, K., S. Maeda, and K. Morokuma. 2019. Roles of closed- and open-loop conformations in large-scale structural transitions of l -lactate dehydrogenase. *ACS Omega.* 4:1178–1184.

70. Peng, Y., C. Zhong, …, J. Ding. 2008. Structural studies of Saccharomyces cerevesiae mitochondrial NADP-dependent isocitrate dehydrogenase in different enzymatic states reveal substantial conformational changes during the catalytic reaction. *Protein Sci.* 17:1542–1554.

71. Costa, C. H. S. d., T. W. Bichara, …, J. Lameira. 2021. Unraveling the conformational dynamics of glycerol 3-phosphate dehydrogenase, a nicotinamide adenine dinucleotide-dependent enzyme of Leishmania mexicana. *J. Biomol. Struct. Dyn.* 39:2044–2055.

72. Oide, M., T. Kato, T. Oroguchi, and M. Nakasako. 2020. Energy landscape of domain motion in glutamate dehydrogenase deduced from cryo-electron microscopy. *FEBS J.* 287:3472–3493.

73. Akai, S., H. Ikushiro, …, I. Miyahara. 2019. The crystal structure of homoserine dehydrogenase complexed with l-homoserine and NADPH in a closed form. *J. Biochem.* 165:185–195.

74. Shimozawa, Y., T. Himiyama, …, Y. Nishiya. 2021. Structural analysis and reaction mechanism of malate dehydrogenase from Geobacillus stearothermophilus. *J. Biochem.* 170:97–105.

75. Plapp, B. V., B. R. Savarimuthu, …, S. Ramaswamy. 2017. Horse liver alcohol dehydrogenase: zinc coordination and catalysis. *Biochemistry.* 56:3632–3646.

76. Zhadin, N., M. Gulotta, and R. Callender. 2008. Probing the role of dynamics in hydride transfer catalyzed by lactate dehydrogenase. *Biophys. J.* 95:1974–1984.

77. Ranjit, S., L. Malacrida, …, E. Gratton. 2019. Determination of the metabolic index using the fluorescence lifetime of free and bound nicotinamide adenine dinucleotide using the phasor approach. *J. Biophot.* 12:e201900156.

78. Neves, R. P. P., P. A. Fernandes, and M. J. Ramos. 2016. Unveiling the catalytic mechanism of NADP+-Dependent isocitrate dehydrogenase with QM/MM calculations. *ACS Catal.* 6:357–368.

79. Peng, H. L., and R. Callender. 2017. Mechanistic analysis of fluorescence quenching of reduced nicotinamide adenine dinucleotide by oxamate in lactate dehydrogenase ternary complexes. *Photochem. Photobiol.* 93:1193–1203.

80. Sanderson, M. J., I. Smith, …, M. D. Bootman. 2014. Fluorescence microscopy. *Cold Spring Harb. Protoc.* 2014. https://doi.org/10.1101/pdb.top071795.

81. Algar, W. R., N. Hildebrandt, …, I. L. Medintz. 2019. FRET as a biomolecular research tool — understanding its potential while avoiding pitfalls. *Nat. Methods.* 16:815–829.

82. Elson, D., J. Requejo-Isidro, …, P. French. 2004. Time-domain fluorescence lifetime imaging applied to biological tissue. *Photochem. Photobiol. Sci.* 3:795–801.

Biophysical Journal, Volume *122*

Supplemental information

NAD(P)H binding configurations revealed by time-resolved fluorescence and two-photon absorption

Thomas S. Blacker, Michael R. Duchen, and Angus J. Bain

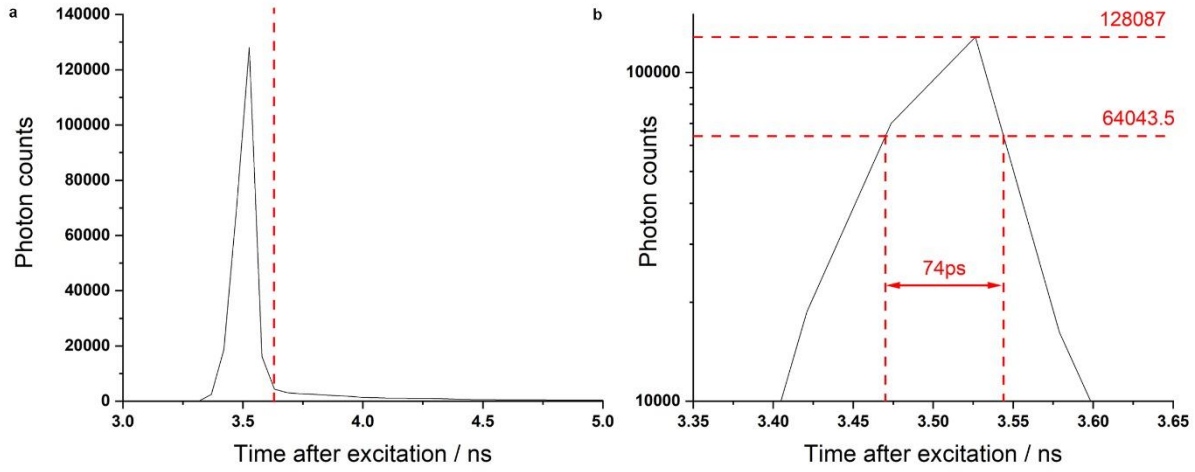

Figure S1: The instrument response function (IRF) associated with our measurements was determined by performing TCSPC at 340nm on NADH added to a saturated solution of potassium iodide, a highly effective quencher(1). This revealed the FWHM of the response to be 74ps. A small tail after the peak (from 3.6ns onwards) could be fit to a biexponential decay with decay constants of 0.47(±0.02) ns and 4.0(±0.1) ns with relative amplitudes of 99.98(±0.01)% and 0.02(±0.01)%. This suggested it to originate primarily from residual unquenched NADH with a characteristic lifetime of 0.4-0.5ns. The longer lifetime minority species may have originated from the potassium iodide itself, which can absorb in the near-UV and fluoresce in the 364-600nm emission window utilised(2).

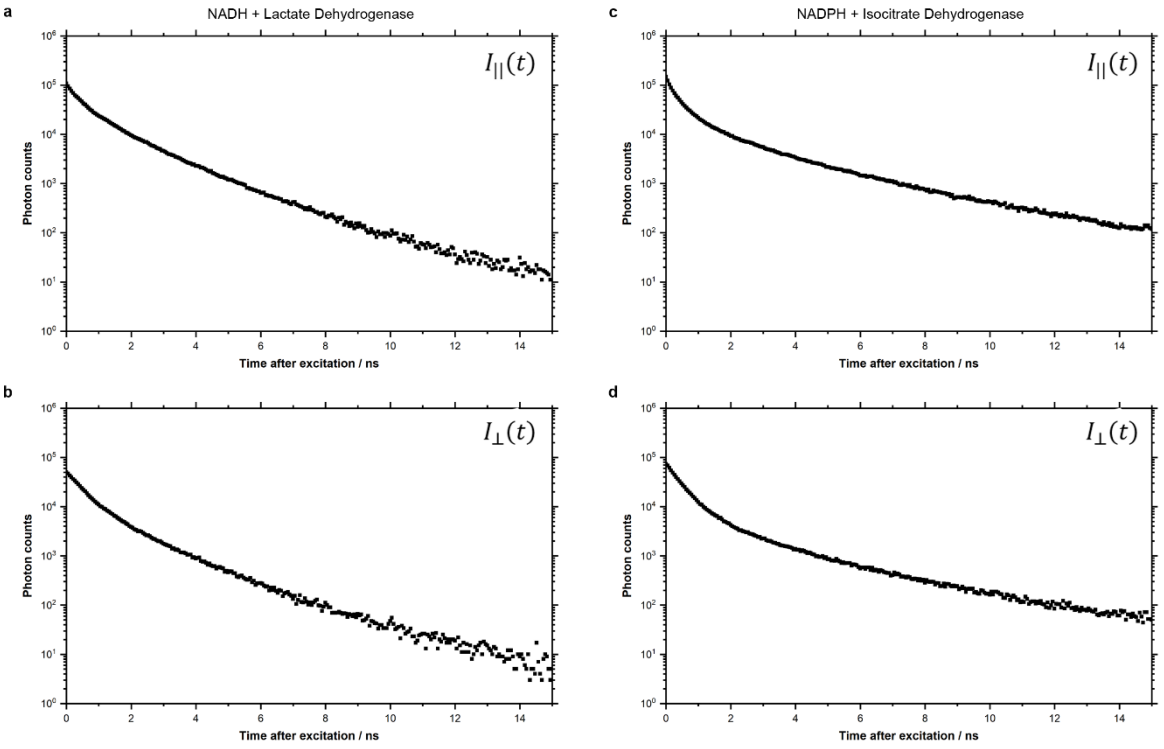

Figure S2: The polarised fluorescence decays $I_{||}(t)$ and $I_{\perp}(t)$, from which the total intensity $I(t)$ and anisotropy $R(t)$ decays were calculated using Equations 1 and 3, for (a & b) NADH mixed with lactate dehydrogenase and (c & d) NADPH mixed with isocitrate dehydrogenase.

Appendix S1

Maximum likelihood fitting of two-photon fluorescence intensity decays

Despite least-squares global fits to the two-photon fluorescence intensity decays giving low χ_R^2 values, the residuals were systematically offset from zero (Figure S3). This suggested an underlying discrepancy between the fitting model and the experimental data, reducing our confidence in the accuracy of the fluorescence decay parameters extracted. This could result from the variance of the data points being improperly assigned in the least-squares weighting function, despite this method being successful in the single-photon case. A known drawback of the least-squares approach described in the main text is that Equation 5 assumes that the Poisson statistics describing photon counting data can be approximated as Gaussian(3). However, this only applies when the number of photon counts in each bin is above approximately 10(4, 5), as shown in Figure S4.

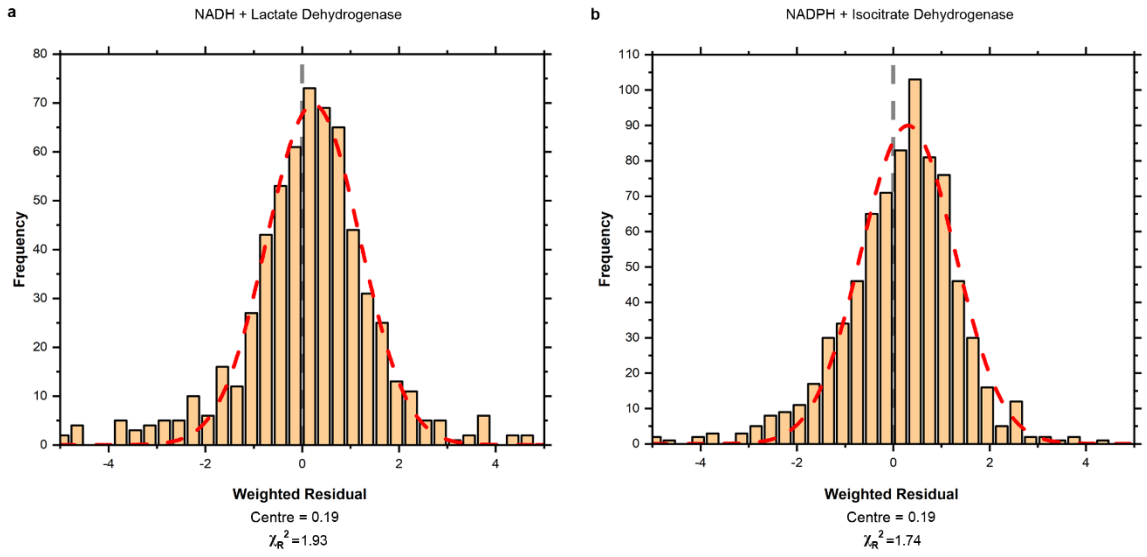

Figure S3: Least-squares fits of a three-component decay model were systematically offset from the time-resolved two-photon fluorescence data. These global fits, in which the three lifetimes were shared between the datasets obtained using linearly and circularly polarised excitation, resulted in acceptable χ_R^2 values. However, the arithmetic means of the weighted residuals were offset from zero, suggesting the fit parameters may be inaccurate.

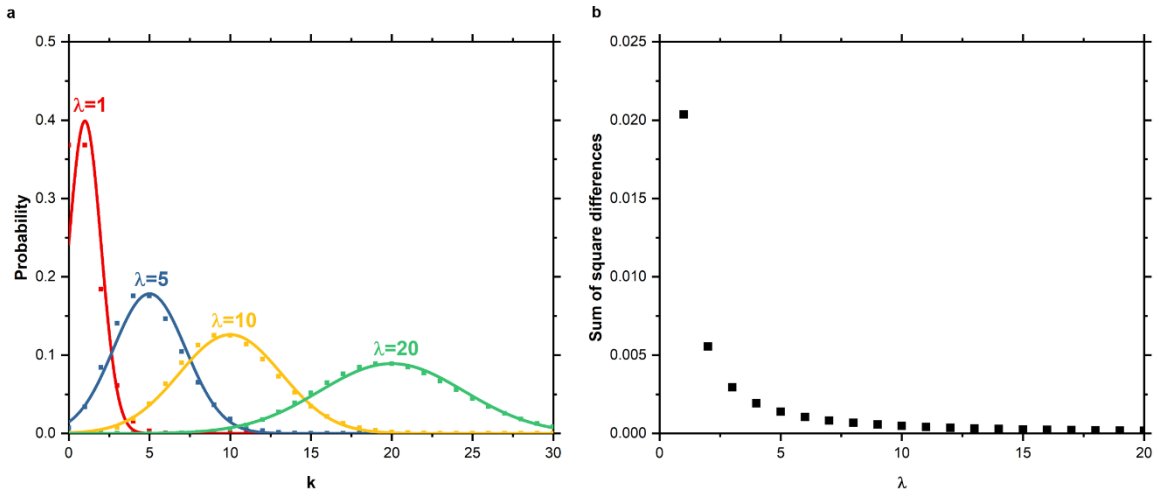

Figure S4: (a) A comparison of the Poisson (points) and Gaussian (lines) distributions, describing the probability of measuring k counts for an expected occurrence rate λ. The similarity of the two distributions increases with λ, as quantified in (b) by the sum of square differences between the distributions.

The lower count rates resulting from two-photon excitation combined with the extended (27ns) excitation-emission correlation times available with our apparatus resulted in 34% of the bins containing fewer than 10 counts, in contrast to 0% with single-photon excitation. To account for this, the maximum likelihood approach can be applied(3, 6–8). Here the fitting algorithm aims to minimise a χ_R^2 based on the likelihood function,

$$\chi_R^2 = \frac{2}{n-l}\sum_{k=1}^{n}\left\{I_{\text{measured}}(t_k)\ln\left[\frac{I_{\text{measured}}(t_k)}{I_{\text{model}}(t_k)}\right] - [I_{\text{measured}}(t_k) - I_{\text{model}}(t_k)]\right\} \quad \text{(S1)}$$

with the magnitude of the residuals given by,

$$|x_k| = \sqrt{2\left\{I_{\text{measured}}(t_k)\ln\left[\frac{I_{\text{measured}}(t_k)}{I_{\text{model}}(t_k)}\right] - [I_{\text{measured}}(t_k) - I_{\text{model}}(t_k)]\right\}} \quad \text{(S2)}$$

and their sign reflecting $I_{\text{measured}}(t_k) - I_{\text{model}}(t_k)$.

This method will underestimate the variance of each datapoint in our experiments as our $I(t)$ data is reconstructed from the addition of polarised decays according to Equation 1, not from

single magic angle measurements. This renders the statistics of the datasets non-Poissonian resulting in the return of quantitatively incorrect χ_R^2 values and preventing the calculation of 95% confidence intervals as per the least squares fits. Quoted uncertainties (see Table S1) are therefore standard deviations calculated from the variance-covariance matrix, which will underestimate the true confidence intervals. Nevertheless, this approach now provided fits with evenly distributed residuals (Figure S5), thereby correcting for the unsatisfactory fits obtained with least squares methods.

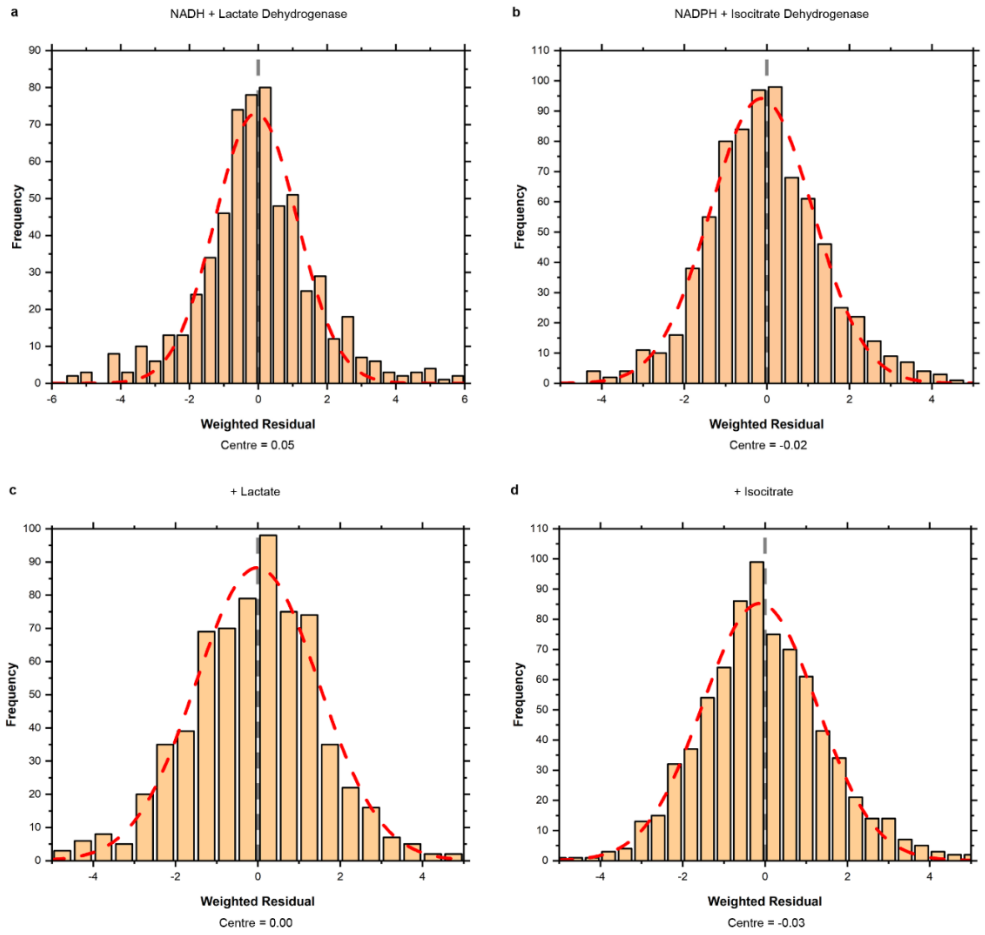

Figure S5: Maximum likelihood fitting to the experimental two-photon fluorescence decay data improved the distribution of the residuals in comparison to weighted least-squares. The likelihood function will underestimate the variance of the data as I_V and I_H were obtained separately in our experiments, meaning the absolute values of χ_R^2 associated with Equation S1 will be larger than their true value.

Appendix S2

Rejection of alternative models for the anisotropy decay of NAD(P)H enzyme mixtures

To confirm the validity of the model described by Equation 16, we compared its performance with both simpler and more complex models. First, we assessed a model in which local motion of the nicotinamide was neglected, with the free species exhibiting a fast rotational correlation time and the two bound species sharing a slower rotational correlation time,

$$R(t) = \frac{R(0)}{\alpha_1 e^{-t/\tau_1} + \alpha_2 e^{-t/\tau_2} + \alpha_3 e^{-t/\tau_3}} \Big(\alpha_1 e^{-t/\tau_1} e^{-t/\tau_{\text{fast}}^{\text{rot}}} + e^{-t/\tau_{\text{slow}}^{\text{rot}}} \{ \alpha_2 e^{-t/\tau_2} + \alpha_3 e^{-t/\tau_3} \} \Big) \tag{S3}$$

Fitting of this model gave evenly distributed residuals, but poorer values of χ_R^2 in comparison to the local motion model, at 3.09 for NADH and lactate dehydrogenase and 3.11 for NADPH and isocitrate dehydrogenase. Furthermore, it performed poorly when assessing the physical validity of the parameters output. $\tau_{\text{slow}}^{\text{rot}}$ was 55(±9) ns for lactate dehydrogenase and 160(±40) ns for isocitrate dehydrogenase. By the Stokes-Einstein-Debye equation, the ratio of these correlation times should follow(9),

$$\frac{\tau_{\text{slow}}^{\text{IDH}}}{\tau_{\text{slow}}^{\text{LDH}}} = \frac{(f\kappa V_h)_{\text{IDH}}}{(f\kappa V_h)_{\text{LDH}}} \tag{S4}$$

The form factor f is 1 for a sphere and deviates above or below this value for increasingly non-spherical shapes. κ varies between 0 and 1 depending on the degree of interaction between protein and solvent. Assuming equal protein densities, the ratio of hydrodynamic volumes for isocitrate dehydrogenase to lactate dehydrogenase can be approximated to their molecular weight ratio of 1.3, whereas the ratio of slow rotational correlation times here was 2.5(±0.5). It is unlikely that κ will differ drastically between the two enzymes, as all proteins are typically surrounded by an extended hydration shell(10). Furthermore, crystal structures of lactate

dehydrogenase and isocitrate dehydrogenase(11, 12) do not imply either has a highly oblate or prolate form ($f \sim 1$). Equation S3 therefore produced physically unrealistic results. In contrast, the ratio of slow rotational correlation times output by the model that accounted for local motion of the nicotinamide (Equation 16) was 1.3(±0.7), in agreement with their ratio of molecular weights, supporting its validity.

The satisfactory fits by Equation 16 implied that the initial anisotropy is equal for each species close to the theoretical maximum of 0.4. To confirm this, we altered this model to include a separate $R(0)$ for each component of the decay. This did not alter the χ_R^2 for the fit, thereby providing no statistical justification for accepting this more complex model. Furthermore, the resulting initial anisotropies were essentially unchanged, with values of 0.38(±0.01) and 0.39(±0.01) for the free species in the NADH and NADPH mixtures respectively, and 0.40(±0.01) for each bound species. While this may imply that a small difference between the absorption and emission transition dipole moments in the free cofactor is eliminated by enzyme binding, this cannot be fully confirmed at the current level of experimental accuracy.

Appendix S3

Identification of potential artefacts induced by tail fitting of decay data

To critically assess the use of the "tail fitting" approach, we performed numerical simulations in MATLAB (The MathWorks, Natick MA, USA). The population and rotational decay dynamics associated with the NADH and lactate dehydrogenase mixture (see Tables 1 and 2) were used to generate separate polarised fluorescence decays using,

$$I_{||}(t) = \frac{I(t)}{3}[1 + 2R(t)] \tag{S5}$$

$$I_{\perp}(t) = \frac{I(t)}{3}[1 - R(t)] \tag{S6}$$

These were each convolved with Gaussian IRFs with FWHMs varying from 0 to 200ps, scaled such that $I_{\max} = 207691$ (to reflect our experimental measurements) and Poisson noise added using the poissrnd() command. The decays were then fit in the manner described in the Methods section. This was repeated 100 times at each FWHM and the results compared with the underlying decay parameters, displayed in Figure S6.

The average intensity decay amplitudes were close (with 3%) to their true values at all IRF widths. This was also the case for the two shorter fluorescence lifetimes τ_1 and τ_2, the means of the 100 repeats being at most 85ps from the underlying value. The spread of τ_3 values returned was much larger than the other intensity decay parameters (at most 550ps), presumably because of its small amplitude and therefore low contribution to the overall signal. As such, at two IRF widths, the average τ_3 value returned was well above (0.8-0.9ns) the true value. However, this appeared unlikely to be a systematic effect of tail fitting given it occurred at a FWHM of 125ps but not 150ps or 175ps, and the lifetime in question was over 15 times larger than these values.

The distinction in restricted rotational diffusion between the two bound species ($B_2 > B_3$) could be identified at all IRF widths. In each case, B_3 was correctly assigned as zero. The mean values of B_2 were slightly lower than the true underlying value. Up to a FWHM of 125ps, these averaged 0.155 relative to the true value of 0.17, with which the spread of each dataset overlapped. A systematic underestimate of B_2 may be evident beyond these values. This could be associated with a systematically underestimated correlation time associated with this motion at IRF widths of 125ps and above and overestimates of the correlation time of unbound species which increased from 0.15ns above the true value at a FWHM of 125ps to 0.28ns at 200ps.

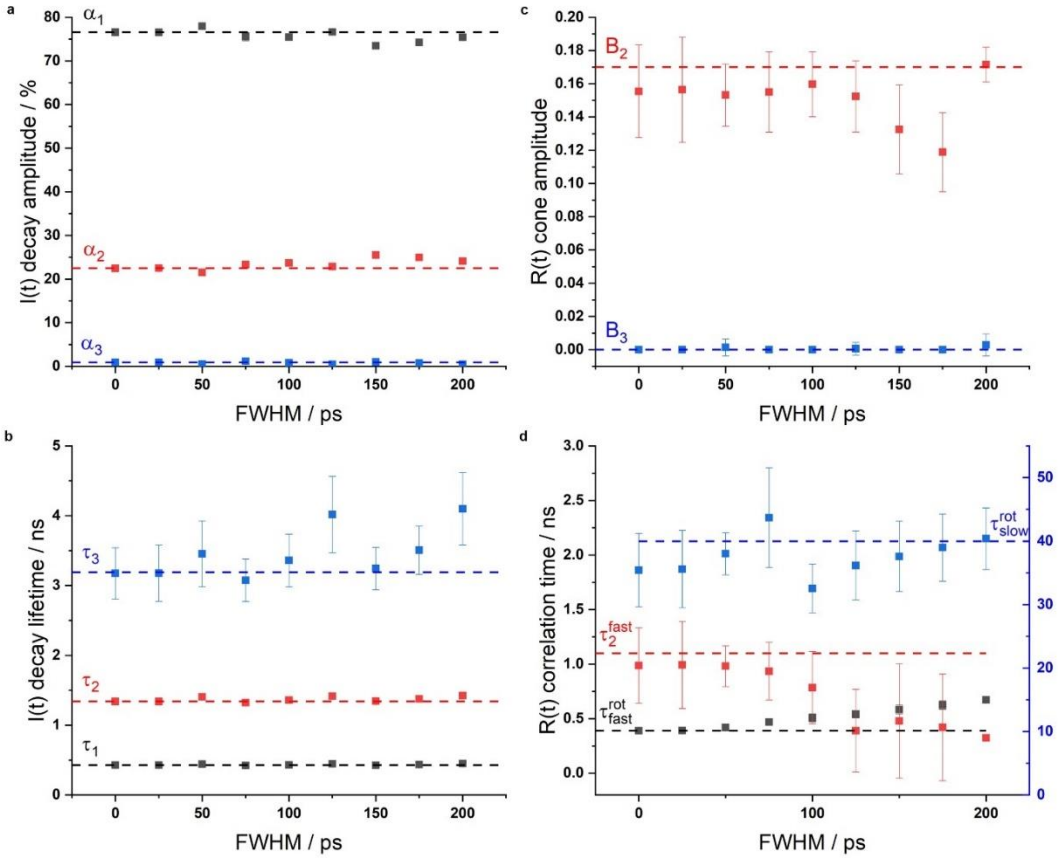

Figure S6: Parameters obtained by tail fitting 100 simulated intensity and anisotropy decay datasets at different Gaussian IRF widths. Dashed lines represent the true underlying parameters.

Table S1

Polarised two-photon fluorescence parameters of NADH mixed with lactate dehydrogenase and NADPH mixed with isocitrate dehydrogenase, and in ternary complexes

	NADH+LDH	+ Lactate	NADPH+IDH	+ Isocitrate
$\overline{\Omega}$	1.04(±0.01)	1.07(±0.01)	0.94(±0.01)	0.97(±0.01)
τ_1 / ns	0.2(±0.4)	0.2(±0.3)	0.26(±0.04)	0.2(±0.3)
τ_2 / ns	1.1(±0.1)	1.3(±0.1)	1.0(±0.3)	1.0(±0.1)
τ_3 / ns	2.4(±0.6)	3.1(±0.1)	4(±1)	4(±1)
α_1^{lin} / %	21(±1)	5(±2)	58(±1)	59(±1)
α_1^{circ} / %	9(±1)	2(±1)	44.1(±0.6)	24(±1)
α_2^{lin} / %	69(±1)	61(±2)	38.9(±0.6)	39(±1)
α_2^{circ} / %	87(±4)	74(±2)	53.9(±0.7)	74(±1)
α_3^{lin} / %	10(±2)	34(±2)	3(±2)	2(±1)
α_3^{circ} / %	4(±5)	24(±2)	2(±1)	2(±1)
$\langle\tau_{\mathrm{lin}}\rangle$ / ns	1.1(±0.1)	1.8(±0.1)	0.6(±0.1)	0.6(±0.1)
$\langle\tau_{\mathrm{circ}}\rangle$ / ns	1.1(±0.2)	1.7(±0.1)	0.7(±0.2)	0.8(±0.1)

Appendix S4

Quantitative analysis of dehydrogenase reaction dynamics

The dehydrogenase reaction mechanism has been extensively studied by Callender and colleagues(13–26) and is described by the following scheme,

$$A \underset{k_{-1}}{\overset{k_1}{\rightleftharpoons}} A \cdot Eo \underset{k_{-2}}{\overset{k_2}{\rightleftharpoons}} A \cdot Eo \cdot So \underset{k_{-3}}{\overset{k_3}{\rightleftharpoons}} A \cdot Ec \cdot S \underset{k_{-4}}{\overset{k_4}{\rightleftharpoons}} B \cdot Ec \cdot P \underset{k_{-5}}{\overset{k_5}{\rightleftharpoons}} B \cdot Eo \cdot P \underset{k_{-6}}{\overset{k_6}{\rightleftharpoons}} B \cdot Eo \underset{k_{-7}}{\overset{k_7}{\rightleftharpoons}} B$$

where A is NAD(P)+, B is NAD(P)H, S is the reduced substrate (lactate or isocitrate), P is the oxidised product (pyruvate or α-ketoglutarate) and o and c represent the open and closed conformations of the enzyme E. This gives,

$$\frac{d}{dt}[A] = k_{-1}[A \cdot Eo] - k_1[A][E] \tag{S7}$$

$$\frac{d}{dt}[A \cdot Eo] = k_1[A][E] + k_{-2}[A \cdot Eo \cdot S] - k_{-1}[A \cdot Eo] - k_2[A \cdot Eo][S] \tag{S8}$$

$$\frac{d}{dt}[A \cdot Eo \cdot S] = k_2[A \cdot Eo][S] + k_{-3}[A \cdot Ec \cdot S] - k_{-2}[A \cdot Eo \cdot S] - k_3[A \cdot Eo \cdot S] \tag{S9}$$

$$\frac{d}{dt}[A \cdot Ec \cdot S] = k_3[A \cdot Eo \cdot S] + k_{-4}[B \cdot Ec \cdot P] - k_{-3}[A \cdot Ec \cdot S] - k_4[A \cdot Ec \cdot S] \tag{S10}$$

$$\frac{d}{dt}[B \cdot Ec \cdot P] = k_4[A \cdot Ec \cdot S] + k_{-5}[B \cdot Eo \cdot P] - k_{-4}[B \cdot Ec \cdot P] - k_5[B \cdot Ec \cdot P] \tag{S11}$$

$$\frac{d}{dt}[B \cdot Eo \cdot P] = k_5[B \cdot Ec \cdot P] + k_{-6}[B \cdot Eo][P] - k_{-5}[B \cdot Eo \cdot P] - k_6[B \cdot Eo \cdot P] \tag{S12}$$

$$\frac{d}{dt}[B \cdot Eo] = k_6[B \cdot Eo \cdot P] + k_{-7}[B \cdot Eo] - k_{-6}[B \cdot Eo][P] - k_7[B \cdot Eo] \tag{S13}$$

$$\frac{d}{dt}[B] = k_7[B \cdot Eo] - k_{-7}[B][E] \tag{S14}$$

The relative abundances of the fluorescent $[B \cdot Eo]$, $[B \cdot Eo \cdot P]$ and $[B \cdot Ec \cdot P]$ species for NAD- and NADP-associated enzymes would dictate the lifetimes we observe for bound NADH and bound NADPH inside cells. At steady state, these are given by,

$$\frac{[B \cdot Eo]}{[B \cdot Eo] + [B \cdot Eo \cdot P] + [B \cdot Ec \cdot P]} = \frac{1}{1 + \frac{k_{-6}}{k_6}[P] + \frac{k_{-5}}{k_5}\frac{k_{-6}}{k_6}[P]} \quad \text{(S15)}$$

$$\frac{[B \cdot Eo \cdot P]}{[B \cdot Eo] + [B \cdot Eo \cdot P] + [B \cdot Ec \cdot P]} = \frac{\frac{k_{-6}}{k_6}[P]}{1 + \frac{k_{-6}}{k_6}[P] + \frac{k_{-5}}{k_5}\frac{k_{-6}}{k_6}[P]} \quad \text{(S16)}$$

$$\frac{[B \cdot Ec \cdot P]}{[B \cdot Eo] + [B \cdot Eo \cdot P] + [B \cdot Ec \cdot P]} = \frac{\frac{k_{-5}}{k_5}\frac{k_{-6}}{k_6}[P]}{1 + \frac{k_{-6}}{k_6}[P] + \frac{k_{-5}}{k_5}\frac{k_{-6}}{k_6}[P]} \quad \text{(S17)}$$

Using temperature jump spectroscopy on lactate dehydrogenase in solution, Zhadin et al. have measured the relative rate of closing and opening of the product-bound enzyme complex k_{-5}/k_5 as 3(±2)(18). Using this value, we can plot in Figure S7 how the relative abundances of the three bound NAD(P)H species relate to the rate of association and dissociation of the product from the NAD(P)H-bound enzyme $k_{-6}[P]/k_6$.

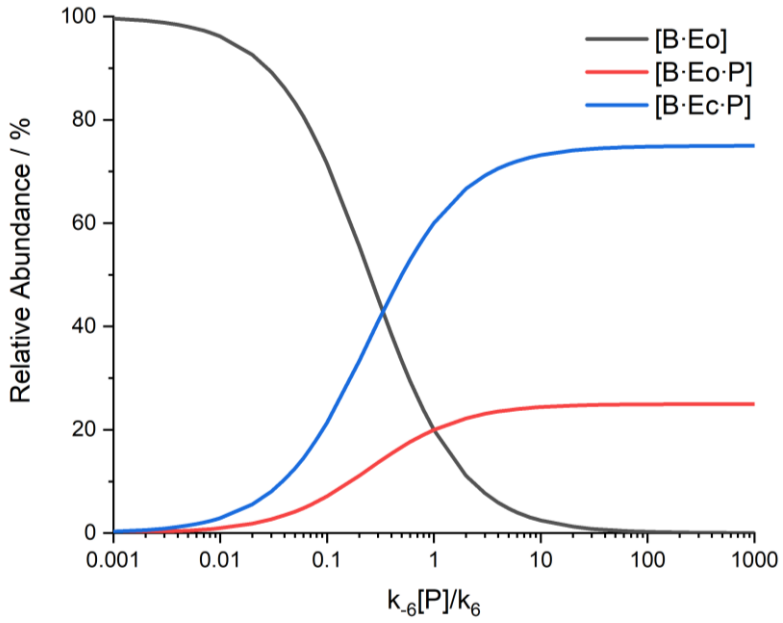

Figure S7: The relative abundance of the three bound NAD(P)H species in Equations S15 to S17 plotted as a function of the relative rate of association and dissociation of the reaction product from the enzyme, $k_{-6}[P]/k_6$, with k_{-5}/k_5 set to 3, as determined experimentally for lactate dehydrogenase.

Figure S7 demonstrates that an increased affinity of the product for the enzyme (higher $k_{-6}[P]/k_6$) leads to a greater abundance of ternary complex enzymes. In our measurements, only the closed conformation of these had a lifetime large enough to reflect the 4.4(±0.2)ns fluorescence lifetime of intracellular bound NADPH. This implies that $k_{-6}[P]/k_6$ is greater for NADPH- than NADH-associated dehydrogenases inside cells.

We note that, as $k_{-6}[P]/k_6 \to \infty$, the relative proportion of $[B \cdot Eo \cdot P]$ and $[B \cdot Ec \cdot P]$ asymptotically approach 25% and 75% respectively. Our measurements suggest these two species would have lifetimes of 1.7ns and 5.3ns for NADPH, giving a concentration weighted average lifetime of 4.4 ns, in exact agreement with our estimate of the fluorescence lifetime of bound NADPH inside cells. In contrast, as $k_{-6}[P]/k_6 \to 0$, the relative proportion of the $[B \cdot Eo]$ species approaches 100%. For NADH, our measurements suggest this corresponds to a lifetime of 1.34ns, within the 0.2ns error bounds of our 1.5ns estimate for its bound intracellular fluorescence lifetime.

Measurements on lactate dehydrogenase(27) have determined a value of $k_{-6}/k_6 = 1.1(\pm 0.4)$ x 10^4 M^{-1} in solution(18). At $[P] = 239$ µM, based on previous cellular pyruvate measurements, the relative weightings of the $[B \cdot Eo]$, $[B \cdot Eo \cdot P]$ and $[B \cdot Ec \cdot P]$ species would be 8.7%, 22.8% and 68.5% according to Equations S15 to S17. Using the lifetime values we measured for each species, these relative proportions would give an average bound lifetime for NADH of 3.0ns, much larger than that we observed inside living cells. This implies that one or more of the rates measured in solution may not apply inside the cell for NADH-associated reactions. k_{-5}, k_5 and k_6 may be more likely to be valid, given that they concern internal transitions within the protein rather than interactions with the environment. There is, however, a growing consensus that constants such as k_{-6}, governing diffusion-limited processes, can be substantially different within the complex, crowded and viscous intracellular milieu(28–33).

An alternative explanation for this disagreement is the neglect of two potentially significant phenomena by this model. Firstly, while the measurements we performed on ternary complexes utilised reduced substrates to ensure no oxidation of NADH and NADPH, there is evidence that the oxidised substrates (e.g. pyruvate, α-ketoglutarate) can quench the fluorescence of the reduced cofactors by providing an acceptor for photoinduced electron transfer(25). This would result in a fluorescence lifetime smaller than that we measured for NAD(P)H in ternary complex with the reduced substrate. Secondly, the model includes only the chain of configurations participating in the catalytic process of the enzyme, but catalytically unproductive configurations can also occur. The binding of reduced substrates alongside reduced cofactors (the so-called "abortive complex") plays a significant role in the regulation of dehydrogenases(34, 35), and the closed enzyme configuration can occur in the absence of substrate, blocking its binding(26). We therefore integrated these phenomena into our model by adding the side reactions,

$$A \cdot Eo \underset{k_{-i}}{\overset{k_i}{\rightleftharpoons}} A \cdot Eo \cdot P \underset{k_{-j}}{\overset{k_j}{\rightleftharpoons}} A \cdot Ec \cdot P$$

$$A \cdot Eo \underset{k_{-k}}{\overset{k_k}{\rightleftharpoons}} A \cdot Ec$$

$$B \cdot Eo \underset{k_{-x}}{\overset{k_x}{\rightleftharpoons}} B \cdot Eo \cdot S \underset{k_{-y}}{\overset{k_y}{\rightleftharpoons}} B \cdot Ec \cdot S$$

$$B \cdot Eo \underset{k_{-z}}{\overset{k_z}{\rightleftharpoons}} B \cdot Ec$$

Repeating the steady state analysis as above gives the following relative weighting for the six different bound NAD(P)H species,

$$\frac{[B \cdot Eo]}{[B \cdot Eo] + [B \cdot Eo \cdot P] + [B \cdot Eo \cdot S] + [B \cdot Ec \cdot P] + [B \cdot Ec \cdot S] + [B \cdot Ec]} = \frac{1}{1 + \frac{k_{-6}}{k_6}[P] + \frac{k_x}{k_{-x}}[S] + \frac{k_{-5}}{k_5}\frac{k_{-6}}{k_6}[P] + \frac{k_x}{k_{-x}}\frac{k_y}{k_{-y}}[S] + \frac{k_z}{k_{-z}}} \quad \text{(S18)}$$

$$\frac{[B \cdot Eo \cdot P]}{[B \cdot Eo] + [B \cdot Eo \cdot P] + [B \cdot Eo \cdot S] + [B \cdot Ec \cdot P] + [B \cdot Ec \cdot S] + [B \cdot Ec]} = \frac{\frac{k_{-6}}{k_6}[P]}{1 + \frac{k_{-6}}{k_6}[P] + \frac{k_x}{k_{-x}}[S] + \frac{k_{-5}}{k_5}\frac{k_{-6}}{k_6}[P] + \frac{k_x}{k_{-x}}\frac{k_y}{k_{-y}}[S] + \frac{k_z}{k_{-z}}} \quad \text{(S19)}$$

$$\frac{[B \cdot Eo \cdot S]}{[B \cdot Eo] + [B \cdot Eo \cdot P] + [B \cdot Eo \cdot S] + [B \cdot Ec \cdot P] + [B \cdot Ec \cdot S] + [B \cdot Ec]} = \frac{\frac{k_x}{k_{-x}}[S]}{1 + \frac{k_{-6}}{k_6}[P] + \frac{k_x}{k_{-x}}[S] + \frac{k_{-5}}{k_5}\frac{k_{-6}}{k_6}[P] + \frac{k_x}{k_{-x}}\frac{k_y}{k_{-y}}[S] + \frac{k_z}{k_{-z}}} \quad \text{(S20)}$$

$$\frac{[B \cdot Ec \cdot P]}{[B \cdot Eo] + [B \cdot Eo \cdot P] + [B \cdot Eo \cdot S] + [B \cdot Ec \cdot P] + [B \cdot Ec \cdot S] + [B \cdot Ec]} = \frac{\frac{k_{-5}}{k_5}\frac{k_{-6}}{k_6}[P]}{1 + \frac{k_{-6}}{k_6}[P] + \frac{k_x}{k_{-x}}[S] + \frac{k_{-5}}{k_5}\frac{k_{-6}}{k_6}[P] + \frac{k_x}{k_{-x}}\frac{k_y}{k_{-y}}[S] + \frac{k_z}{k_{-z}}} \quad \text{(S21)}$$

$$\frac{[B \cdot Ec \cdot S]}{[B \cdot Eo] + [B \cdot Eo \cdot P] + [B \cdot Eo \cdot S] + [B \cdot Ec \cdot P] + [B \cdot Ec \cdot S] + [B \cdot Ec]} = \frac{\frac{k_x}{k_{-x}}\frac{k_y}{k_{-y}}[S]}{1 + \frac{k_{-6}}{k_6}[P] + \frac{k_x}{k_{-x}}[S] + \frac{k_{-5}}{k_5}\frac{k_{-6}}{k_6}[P] + \frac{k_x}{k_{-x}}\frac{k_y}{k_{-y}}[S] + \frac{k_z}{k_{-z}}} \quad \text{(S22)}$$

$$\frac{[B \cdot Ec]}{[B \cdot Eo] + [B \cdot Eo \cdot P] + [B \cdot Eo \cdot S] + [B \cdot Ec \cdot P] + [B \cdot Ec \cdot S] + [B \cdot Ec]} = \frac{\frac{k_z}{k_{-z}}}{1 + \frac{k_{-6}}{k_6}[P] + \frac{k_x}{k_{-x}}[S] + \frac{k_{-5}}{k_5}\frac{k_{-6}}{k_6}[P] + \frac{k_x}{k_{-x}}\frac{k_y}{k_{-y}}[S] + \frac{k_z}{k_{-z}}} \quad \text{(S23)}$$

To simplify this preliminary analysis, we assume that the rates governing the transition between open and closed enzyme states are equal in the presence of both (oxidised) products $[P]$ and (reduced) substrates $[S]$ ($k_y/k_{-y} = k_{-5}/k_5$) and that the rates of binding and unbinding of product and substrate to the open conformation NAD(P)H-bound enzyme are equal ($k_x/k_{-x} = k_{-6}/k_6$). We will also assume that the fluorescence lifetimes of NAD(P)H in the open conformation ternary complexes are identical, regardless of whether product or substrate is bound. Finally, to relate the relative proportions of each species back to the contrasting intracellular biochemistry of the NAD and NADP pools, we will replace the relative concentrations of $[P]$ and $[S]$ with the redox balance of the associated cofactor pool using the equilibrium constant(36, 37),

$$\frac{[P]}{[S]} = K_{\mathrm{eq}} \frac{[A]}{[B]} \tag{S24}$$

Introducing these simplifications into Equations S18 to S23, writing the total concentration of substrates and products as $[T]$, gives,

$$\frac{[B \cdot Eo]}{[B \cdot Eo] + [B \cdot Eo \cdot P] + [B \cdot Eo \cdot S] + [B \cdot Ec \cdot P] + [B \cdot Ec \cdot S] + [B \cdot Ec]} = \frac{\frac{1}{[T]}}{\frac{1}{[T]}\left(1 + \frac{k_z}{k_{-z}}\right) + \frac{k_{-6}}{k_6}\left(1 + \frac{k_{-5}}{k_5}\right)} \tag{S25}$$

$$\frac{[B \cdot Eo \cdot P] + [B \cdot Eo \cdot S]}{[B \cdot Eo] + [B \cdot Eo \cdot P] + [B \cdot Eo \cdot S] + [B \cdot Ec \cdot P] + [B \cdot Ec \cdot S] + [B \cdot Ec]} = \frac{\frac{k_{-6}}{k_6}}{\frac{1}{[T]}\left(1 + \frac{k_z}{k_{-z}}\right) + \frac{k_{-6}}{k_6}\left(1 + \frac{k_{-5}}{k_5}\right)} \tag{S26}$$

$$\frac{[B \cdot Ec \cdot P]}{[B \cdot Eo] + [B \cdot Eo \cdot P] + [B \cdot Eo \cdot S] + [B \cdot Ec \cdot P] + [B \cdot Ec \cdot S] + [B \cdot Ec]}$$

$$= \frac{\frac{k_{-5}}{k_5}\frac{k_{-6}}{k_6}\left(\frac{K_{\mathrm{eq}}\,[A]/[B]}{1 + K_{\mathrm{eq}}\,[A]/[B]}\right)}{\frac{1}{[T]}\left(1 + \frac{k_z}{k_{-z}}\right) + \frac{k_{-6}}{k_6}\left(1 + \frac{k_{-5}}{k_5}\right)} \quad \text{(S27)}$$

$$\frac{[B \cdot Ec \cdot S]}{[B \cdot Eo] + [B \cdot Eo \cdot P] + [B \cdot Eo \cdot S] + [B \cdot Ec \cdot P] + [B \cdot Ec \cdot S] + [B \cdot Ec]}$$

$$= \frac{\frac{k_{-5}}{k_5}\frac{k_{-6}}{k_6}\left(\frac{1}{1 + K_{\mathrm{eq}}\,[A]/[B]}\right)}{\frac{1}{[T]}\left(1 + \frac{k_z}{k_{-z}}\right) + \frac{k_{-6}}{k_6}\left(1 + \frac{k_{-5}}{k_5}\right)} \quad \text{(S28)}$$

$$\frac{[B \cdot Ec]}{[B \cdot Eo] + [B \cdot Eo \cdot P] + [B \cdot Eo \cdot S] + [B \cdot Ec \cdot P] + [B \cdot Ec \cdot S] + [B \cdot Ec]}$$

$$= \frac{\frac{1}{[T]}\frac{k_z}{k_{-z}}}{\frac{1}{[T]}\left(1 + \frac{k_z}{k_{-z}}\right) + \frac{k_{-6}}{k_6}\left(1 + \frac{k_{-5}}{k_5}\right)} \quad \text{(S29)}$$

In Figure S8, we plot Equations S25 to S29 as a function of $K_{\mathrm{eq}}\,[A]/[B]$ to understand how the redox balance of the cofactor pool may relate to the relative abundances of each enzyme bound species. k_{-5}/k_5 and k_{-6}/k_6 were set at 3 and 1.1 x 10^4 M^{-1} respectively, based on the experimental measurements described above(18). k_z/k_{-z} was estimated as 0.095, an average of the 0.04 and 0.15 values of the α_3/α_2 ratios in our binary complex measurements for NADH and NADPH. The concentration scale $[T]$ was chosen as 1mM to reflect the order of magnitude of intracellular redox couples(27).

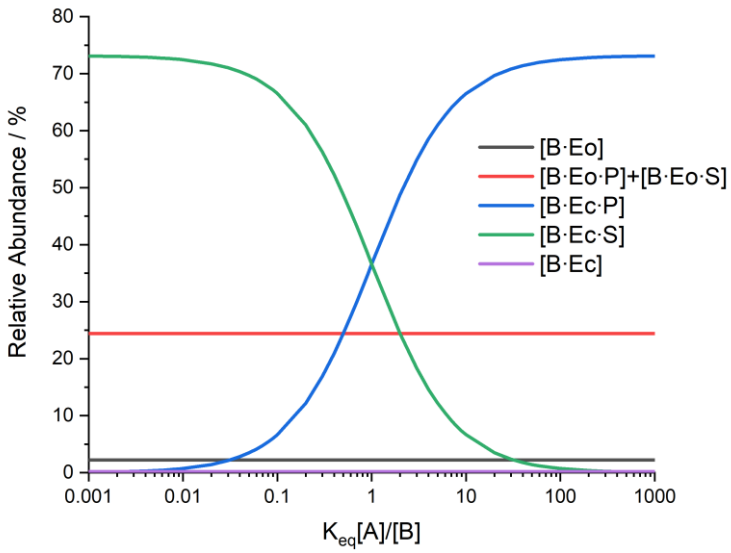

Figure S8: The relative abundance of the five bound NAD(P)H species in Equations S25 to S29 plotted against the product of the NAD(P) redox balance, $[A]/[B]$, and the equilibrium constant K_{eq}. k_{-5}/k_5 and k_{-6}/k_6 were set to the values of 3 and 1.1 x 10^4 M^{-1} respectively, as determined experimentally for lactate dehydrogenase(18). k_z/k_{-z} was set to 0.095, the average of the α_3/α_2 ratios in our measurements of NADH and NADPH in binary complexes. The concentration scale $[T]$ was set to 1mM.

Figure S8 demonstrates that the contributions from open and closed binary complexes remain constant with cofactor redox state, at 2.2% and 0.2% respectively. This is also the case for the combined contribution from open ternary complexes, remaining at 24.4%; a consequence of assuming the fluorescence lifetime of the cofactor to be invariant to the presence of oxidised product or reduced substrate molecules in the open conformation. In contrast, the abortive ternary complex of NAD(P)H with reduced substrate dominates at low values of $K_{\mathrm{eq}}[A]/[B]$, whereas the catalytic ternary complex of NAD(P)H with the oxidised product dominates at high values of $K_{\mathrm{eq}}[A]/[B]$. This could provide a possible mechanism for the difference in the enzyme bound lifetime of NADPH and NADH inside cells where the NADP redox state is

maintained low ($[A]/[B] \ll 1$) and the NAD redox state is maintained high ($[A]/[B] \gg 1$)(36, 38).

In the limit of $K_{\mathrm{eq}}[A]/[B] \to 0$, the contribution from the closed ternary complex with oxidised product goes to zero, corresponding to a concentration-weighted mean bound lifetime of 4.3ns using the fluorescence lifetimes obtained in our experiments on NADPH and isocitrate dehydrogenase (1.6, 1.7, 5.3 and 4.37ns for $[B \cdot Eo]$, $[B \cdot Eo \cdot P] + [B \cdot Eo \cdot S]$, $[B \cdot Ec \cdot S]$ and $[B \cdot Ec]$ respectively). This is within the 0.2ns error bounds of our estimate of the fluorescence lifetime of bound NADPH inside cells of 4.4ns. Given our lack of knowledge of the fluorescence lifetime of NADH in complex with an oxidised product (e.g. pyruvate), it is not possible to carry out similar calculations for $K_{\mathrm{eq}}[A]/[B] \to \infty$. However, to achieve a concentration weighted average lifetime equal to the 1.5ns fluorescence lifetime of bound NADH inside cells, the fluorescence lifetimes obtained in our experiments on NADH and lactate dehydrogenase (1.34, 1.9 and 3.19ns for $[B \cdot Eo]$, $[B \cdot Eo \cdot P] + [B \cdot Eo \cdot S]$ and $[B \cdot Ec]$ respectively) would require excited state quenching by oxidised products to decrease the lifetime of ternary complex NADH to 1.37ns. Relative to the 3.64 ns lifetime of NADH in ternary complex with lactate, this would require a rate of photoinduced electron transfer of 0.46 ns^{-1}, within the range expected for biomolecular systems(39, 40).

It is important to note that these basic models are based on best guesses for the rate constants and neglect any differences in these parameters between NADH- and NADPH-associated enzymes. Nevertheless, they allow a preliminary analysis of the effect of the differing redox states of the NAD and NADP pools on the equilibria of the NAD(P)H-bound enzyme conformations, revealing that the low NADP+/NADPH ratio results in a larger fluorescence lifetime for bound NADPH than bound NADH at a given value of the equilibrium constant due to the increased proportion of abortive ternary complexes.

Supplemental References

1. Hanley, Q.S., V. Subramaniam, D.J. Arndt-Jovin, and T.M. Jovin. 2001. Fluorescence Lifetime Imaging: Multi-point Calibration, Minimum Resolvable Differences, and Artifact Suppression. *Cytometry*. 43:248–260.

2. Teegarden, K.J. 1957. Luminescence of potassium iodide. *Phys. Rev.* 105:1222–1227.

3. Maus, M., M. Cotlet, J. Hofkens, T. Gensch, F.C. De Schryver, J. Schaffer, and C.A.M. Seidel. 2001. An experimental comparison of the maximum likelihood estimation and nonlinear least-squares fluorescence lifetime analysis of single molecules. *Anal. Chem.* 73:2078–2086.

4. Bevington, P.R., and D.K. Robinson. 2003. Data Reduction and Error Analysis for the Physical Sciences. 3rd Edition. McGraw-Hill.

5. Taylor, J. 1997. Introduction to error analysis, the study of uncertainties in physical measurements. University Science Books.

6. Bajzer, Ž., T.M. Therneau, J.C. Sharp, and F.G. Prendergast. 1991. Maximum likelihood method for the analysis of time-resolved fluorescence decay curves. *Eur. Biophys. J.* 20:247–262.

7. Santra, K., J. Zhan, X. Song, E.A. Smith, N. Vaswani, and J.W. Petrich. 2016. What Is the Best Method to Fit Time-Resolved Data? A Comparison of the Residual Minimization and the Maximum Likelihood Techniques As Applied to Experimental Time-Correlated, Single-Photon Counting Data. *J. Phys. Chem. B.* 120:2484–2490.

8. Köllner, M., and J. Wolfrum. 1992. How many photons are necessary for fluorescence-lifetime measurements? *Chem. Phys. Lett.* 200:199–204.

9. Blacker, T.S., R.J. Marsh, M.R. Duchen, and A.J. Bain. 2013. Activated barrier crossing

dynamics in the non-radiative decay of NADH and NADPH. *Chem. Phys.* 422:184–194.

10. Ebbinghaus, S., J.K. Seung, M. Heyden, X. Yu, U. Heugen, M. Gruebele, D.M. Leitner, and M. Havenith. 2007. An extended dynamical hydration shell around proteins. *Proc. Natl. Acad. Sci. U. S. A.* 104:20749–20752.

11. Xu, X., J. Zhao, Z. Xu, B. Peng, Q. Huang, E. Arnold, and J. Ding. 2004. Structures of human cytosolic NADP-dependent isocitrate dehydrogenase reveal a novel self-regulatory mechanism of activity. *J. Biol. Chem.* 279:33946–33957.

12. Friberg, A., H. Rehwinkel, D. Nguyen, V. Pütter, M. Quanz, J. Weiske, U. Eberspächer, I. Heisler, and G. Langer. 2020. Structural Evidence for Isoform-Selective Allosteric Inhibition of Lactate Dehydrogenase A. *ACS Omega*. 5:13034–13041.

13. Deng, H., N. Zhadin, and R. Callender. 2001. Dynamics of protein ligand binding on multiple time scales: NADH binding to lactate dehydrogenase. *Biochemistry*. 40:3767–3773.

14. Deng, H., S. Brewer, D.M. Vu, K. Clinch, R. Callender, and R.B. Dyery. 2008. On the pathway of forming enzymatically productive ligand-protein complexes in lactate dehydrogenase. *Biophys. J.* 95:804–813.

15. Reddish, M.J., H.L. Peng, H. Deng, K.S. Panwar, R. Callender, and R.B. Dyer. 2014. Direct evidence of catalytic heterogeneity in lactate dehydrogenase by temperature jump infrared spectroscopy. *J. Phys. Chem. B.* 118:10854–10862.

16. Reddish, M.J., R. Callender, and R.B. Dyer. 2017. Resolution of Submillisecond Kinetics of Multiple Reaction Pathways for Lactate Dehydrogenase. *Biophys. J.* 112:1852–1862.

17. Zhadin, N., and R. Callender. 2011. Effect of osmolytes on protein dynamics in the lactate dehydrogenase- catalyzed reaction. *Biochemistry*. 50:1582–1589.

18. Zhadin, N., M. Gulotta, and R. Callender. 2008. Probing the role of dynamics in hydride transfer catalyzed by lactate dehydrogenase. *Biophys. J.* 95:1974–1984.

19. Deng, H., D. V. Vu, K. Clinch, R. Desamero, R.B. Dyer, and R. Callender. 2011. Conformational heterogeneity within the Michaelis complex of lactate dehydrogenase. *J. Phys. Chem. B.* 115:7670–7678.

20. Gulotta, M., H. Deng, H. Deng, R.B. Dyer, and R.H. Callender. 2002. Toward an understanding of the role of dynamics on enzymatic catalysis in lactate dehydrogenase. *Biochemistry*. 41:3353–3363.

21. McClendon, S., N. Zhadin, and R. Callender. 2005. The approach to the Michaelis complex in lactate dehydrogenase: The substrate binding pathway. *Biophys. J.* 89:2024–2032.

22. McClendon, S., D.M. Vu, K. Clinch, R. Callender, and R.B. Dyer. 2005. Structural transformations in the dynamics of Michaelis complex formation in lactate dehydrogenase. *Biophys. J.* 89:L07–L09.

23. Peng, H.L., H. Deng, R.B. Dyer, and R. Callender. 2014. Energy landscape of the michaelis complex of lactate dehydrogenase: Relationship to catalytic mechanism. *Biochemistry*. 53:1849–1857.

24. Pineda, J.R.E.T., R. Callender, and S.D. Schwartz. 2007. Ligand binding and protein dynamics in lactate dehydrogenase. *Biophys. J.* 93:1474–1483.

25. Peng, H.L., and R. Callender. 2017. Mechanistic Analysis of Fluorescence Quenching of Reduced Nicotinamide Adenine Dinucleotide by Oxamate in Lactate Dehydrogenase Ternary Complexes. *Photochem. Photobiol.* 93:1193–1203.

26. Qiu, L., M. Gulotta, and R. Callender. 2007. Lactate dehydrogenase undergoes a substantial structural change to bind its substrate. *Biophys. J.* 93:1677–1686.

27. Tischler, M.E., D. Friedrichs, K. Coll, and J.R. Williamson. 1977. Pyridine nucleotide distributions and enzyme mass action ratios in hepatocytes from fed and starved rats. *Arch. Biochem. Biophys.* 184:222–236.

28. Matić, M., S. Saurabh, J. Hamacek, and F. Piazza. 2020. Crowding-Induced Uncompetitive Inhibition of Lactate Dehydrogenase: Role of Entropic Pushing. *J. Phys. Chem. B.* 124:727–734.

29. Wilcox, A.E., M.A. LoConte, and K.M. Slade. 2016. Effects of macromolecular crowding on alcohol dehydrogenase activity are substrate-dependent. *Biochemistry*. 55:3550–3558.

30. Zheng, K., T.P. Jensen, L.P. Savtchenko, J.A. Levitt, K. Suhling, and D.A. Rusakov. 2017. Nanoscale diffusion in the synaptic cleft and beyond measured with time-resolved fluorescence anisotropy imaging. *Sci. Rep.* 7:42022.

31. Molines, A.T., J. Lemière, M. Gazzola, I.E. Steinmark, C.H. Edrington, C.T. Hsu, P. Real-Calderon, K. Suhling, G. Goshima, L.J. Holt, M. Thery, G.J. Brouhard, and F. Chang. 2022. Physical properties of the cytoplasm modulate the rates of microtubule polymerization and depolymerization. *Dev. Cell*. 57:466-479.e6.

32. Ellis, R.J. 2001. Macromolecular crowding: An important but neglected aspect of the intracellular environment. *Curr. Opin. Struct. Biol.* 11:114–119.

33. Minton, A.P. 2006. How can biochemical reactions within cells differ from those in test tubes? *J. Cell Sci.* 119:2863–2869.

34. Fromm, H. 1963. Determination of Dissociation Constants of Coenzymes and Abortive. *J. Biol. Chem.* 238:2938–2944.

35. Eggert, M.W., M.E. Byrne, and R.P. Chambers. 2011. Impact of high pyruvate concentration on kinetics of rabbit muscle lactate dehydrogenase. *Appl. Biochem.*

Biotechnol. 165:676–686.

36. Veech, R.L., L. V. Eggleston, and H.A. Krebs. 1969. The redox state of free nicotinamide-adenine dinucleotide phosphate in the cytoplasm of rat liver. *Biochem. J.* 115:609–619.

37. Williamson, D.H., P. Lund, and H.A. Krebs. 1967. The redox state of free nicotinamide-adenine dinucleotide in the cytoplasm and mitochondria of rat liver. *Biochem. J.* 103:514–527.

38. Sun, F., C. Dai, J. Xie, and X. Hu. 2012. Biochemical issues in estimation of cytosolic free NAD/NADH ratio. *PLoS One.* 7:e34525.

39. Van Den Berg, P.A.W., A. Van Hoek, C.D. Walentas, R.N. Perham, and A.J.W.G. Visser. 1998. Flavin fluorescence dynamics and photoinduced electron transfer in Escherichia coli glutathione reductase. *Biophys. J.* 74:2046–2058.

40. Piotrowiak, P. 1999. Photoinduced electron transfer in molecular systems: Recent developments. *Chem. Soc. Rev.* 28:143–150.